Geochemistry of serpentinized and multiphase altered Atlantis Massif peridotites (IODP Expedition 357): Petrogenesis and discrimination of melt-rock vs. fluid-rock processes

Scott Whattam, Gretchen Früh-Green, Mathilde Cannat, Jan C.M. de Hoog, Esther Schwarzenbach, Javier Escartin, Barbara John, Mathew Leybourne, Morgan Williams, Stéphane Rouméjon, et al.

Geochemistry of serpentinized and multiphase altered Atlantis Massif peridotites (IODP Expedition 357): Petrogenesis and discrimination of melt-rock vs. fluid-rock processes

Scott A. Whattam[a*], Gretchen L. Früh-Green[b], Mathilde Cannat[c], Jan C. M. De Hoog[d], Esther M. Schwarzenbach[e], Javier Escartin[f], Barbara E. John[g], Mathew I. Leybourne[h], Morgan J. Williams[i], Stéphane Rouméjon[b], Norikatsu Akizawa[j], Chiara Boschi[k], Michelle Harris[l], Kirsten Wenzel[m], Andrew McCaig[n], Dominique Weis[o], Laura Bilenker[p]

[a]*Department of Geosciences, King Fahd University of Petroleum and Minerals, Dhahran, 31261, Saudi Arabia*

[b]*Institute of Geochemistry and Petrology, ETH Zurich, Clausiusstrasse 25, 8092 Zürich, Switzerland*

[c]*Institut de Physique du Globe de Paris, CNRS, 1 rue Jussieu, 75238 Paris, Cedex 05, France*

[d]*School of Geosciences, Grant Institute, The University of Edinburgh, James Hutton Road, EH9 3FE, United Kingdom*

[e]*Institute of Geological Sciences, Freie Universität Berlin, Malteserstrasse 74-100, 12249 Berlin, Germany*

[f]*Laboratoire de Géologie – CNRS, UMR 8538, École Normale Supérieure, PSL University, Paris, France*

[g]*Department of Geology and Geophysics, University of Wyoming, Laramie, WY 82071*

[h]*Queen's Facility for Isotope Research, Department of Geological Sciences and Geological Engineering, and Arthur B. McDonald Canadian Astroparticle Physics Research Institute, Department of Physics, Engineering Physics & Astronomy, Queen's University, Kingston, ON, Canada, K7L 3N6*

[i]*CSIRO Mineral Resources, 26 Dick Perry Avenue, Kensington WA 6151, Australia*

[j]*Kanazawa University, Department of Earth Sciences, Kakuma Kanazawa, Ishikawa 920-1192, Japan*

[k]*Institute of Geosciences and Earth Resources – CNR, Via Moruzzi 1, 56124 Pisa, Italy*

[l]*School of Geography, Earth and Environmental Sciences, 109 Fitzroy Building, Plymouth University, Plymouth PL4 8AA, United Kingdom.*

[m]*GeoZentrum Nordbayern, Friedrich-Alexander-University Erlangen-Nuremberg, Schlossgarten 5a, 91054 Erlangen, Germany*

[n]*School of Earth and Environment, Leeds University, Woodhouse, Leeds LS2 9JT, United Kingdom*

[o]*Pacific Centre for Isotopic and Geochemical Research, Earth, Ocean and Atmospheric Sciences, University of British Columbia, Earth, Ocean and Atmospheric Sciences, 2020-2207 Main Mall, Vancouver BC V6T-1Z4, Canada*

[p]*Deparment of Geosciences, Auburn University, Auburn, AL 36849*

[*]Corresponding author: Scott A. Whattam

E-mail address: sawhatta@gmail.com

Abstract

International Ocean Discovery Program (IODP) Expedition 357 drilled 17 shallow sites distributed ~ 10 km in the spreading direction (from west to east) across the Atlantis Massif oceanic core complex (Mid-Atlantic Ridge, 30 ºN). Mantle exposed in the footwall of the Atlantis Massif oceanic core complex is predominantly nearly wholly serpentinized harzburgite with subordinate dunite. Altered peridotites are subdivided into three types: (I) serpentinites, (II) melt-impregnated serpentinites, and (III) metasomatic serpentinites. Type I serpentinites show no evidence of melt-impregnation or metasomatism apart from serpentinization and local oxidation. Type II serpentinites have been intruded by gabbroic melts and are distinguishable in some cases on the basis of macroscopic and microscopic observations, e.g., mm-cm scale mafic-melt veinlets, rare plagioclase (<0.5 modal % in one sample) or by the local presence of secondary (replacive) olivine after orthopyroxene; in other cases, 'cryptic' melt-impregnation is inferred on the basis of incompatible element enrichments. Type III serpentinites are characterized by silica metasomatism manifested by alteration of orthopyroxene to talc and amphibole, and by anomalously high anhydrous SiO_2 concentrations (59-61 wt.%) and low MgO/SiO_2 values (0.48-0.52). Although many chondrite-normalized rare earth element (REE) and primitive mantle-normalized incompatible trace element anomalies, e.g., negative Ce-anomalies, are attributable to serpentinization, other compositional heterogeneities are due to melt-impregnation. On the basis of whole rock incompatible

62 trace elements, a dominant mechanism of melt-impregnation is distinguished in the
63 central and eastern serpentinites from fluid-rock alteration (mostly serpentinization) in
64 the western serpentinites, with increasing melt-impregnation manifest as a west to east
65 increase in enrichment in high-field strength elements and light REE. High degrees of
66 melt extraction are evident in low whole-rock Al_2O_3/SiO_2 values and low concentrations
67 of Al_2O_3, CaO and incompatible elements. Estimates of the degree of melt extraction
68 based on whole rock REE patterns suggest a maximum of ~ 20 % non-modal fractional
69 melting, with little variation between sites. As some serpentinite samples are *ex situ*
70 rubble, the magmatic histories observed at each site are consistent with a local source
71 (from the fault zone) rather than rafted rubble that would be expected to show more
72 heterogeneity and no spatial pattern. In this case, the studied sites may provide a record
73 of enhanced melt-rock interactions with time, consistent with proposed geological
74 models. Alternatively, sites may signify heterogeneities in these processes at spatial scales
75 of a few km.
76
77 *Keywords*: IODP Expedition 357; Atlantis Massif; mantle peridotite; fluid-rock interaction;
78 melt-rock interaction

1. Introduction

Spreading rate exerts a profound influence on the geometry and architecture of the oceanic crust. Slow-spreading ridges (≤ 5 cm/year), as exemplified by the Mid-Atlantic ridge (MAR), are characterized by wide (up to 30 km) and deep (1–2 km) axial valleys bounded by uplifted shoulders and transient magma reserves. In contrast, fast-spreading ridges (≥ 9 cm/year), as characterized by the East Pacific Rise, exhibit much narrower to absent axial troughs (a few hundred meters wide) and a more continuous magma supply (e.g., Macdonald, 1982; Karson, 2002; Stewart et al., 2005). Analogous with 'metamorphic core complexes' found in extended continental regions (e.g., John, 1987), 'oceanic core complexes' (OCCs), such as the Atlantis Massif (30 °N, Fig. 1a) along the MAR, represent segments of a slow spreading ridge comprised of elevated seafloor massifs that display flat or gently curved upper surfaces with prominent corrugations or 'megamullions' (Escartin et al., 2017; Tucholke et al., 1998). OCCs comprise segments of lower crustal and upper mantle rocks exposed at the seafloor (Cann et al., 1997; Blackman et al., 1998; Tucholke et al., 1998) and represent uplifted footwalls of large-offset low-angle normal faults, commonly referred to as detachment faults. Mantle rocks of OCCs characteristically comprise olivine-rich peridotite (i.e., harzburgite, dunite) that interacted with seawater to produce serpentinite over a range of temperatures (Andreani et al., 2007; Blackman et al., 1998; Boschi et al., 2006a; Boschi et al., 2006b; Cann et al., 1997; Cannat, 1993; Früh-Green et al., 2004; Karson et al., 2006; Kelemen et al., 2007; Rouméjon et al., 2015; Rouméjon et al., 2018a; Schroeder et al, 2002).

Four OCCs have been drilled by the Ocean Drilling Program (ODP), the Integrated Ocean Drilling Program (IODP) and the International Ocean Discovery Program (IODP). The Atlantis Massif is one of the best studied and well-known OCC as it hosts the off-axis, peridotite-hosted Lost City hydrothermal field (Kelley et al., 2001)

on its southern wall (Fig. 1b). Other drilled OCCs include the Atlantis Bank, SW Indian Ridge (ODP Hole 735B, Dick et al., 2000), the MARK (Mid-Atlantic Ridge Kane fracture zone) at 23°32′ N (ODP Leg 153, Sites 921–924, Cannat et al., 1995), and an OCC on the MAR at 15°44′ N (ODP Leg 209, Site 1275, Kelemen et al., 2004). The Atlantis Massif (30 °N, Fig. 1a) was drilled during IODP Expeditions 304/305 (Blackman et al., 2006), at Site U1309 and Expedition 357 (Früh-Green et al., 2017, 2018; Roumejon et al., 2018a, 2018b; Akizawa et al., 2020).

Research on detachment faulting at OCCs implies that oceanic spreading is closely linked to the development of hydrothermal circulation patterns and encompasses a wide variety of fluid flow and hydrothermal regimes (McCaig et al., 2007; Escartin et al., 2008). High-temperature fluid circulation both within the footwall and along the fault zone is well documented on the basis of mineralogy and geochemistry (Schroeder and John, 2004; Boschi et al., 2006a; McCaig et al., 2010, Picazo et al., 2012, Verlaguet et al., 2021). Importantly, uplift along detachment faults appears to promote circulation and alteration within the footwall. Several studies propose a temporal evolution in the style of hydrothermal circulation associated with OCC formation. High-temperature systems are hosted in the basaltic hanging wall within the rift valley, whereas high-temperature ultramafic-hosted systems occur within the OCC footwall. Ultimately, hydrothermal circulation transitions to off-axis ultramafic-hosted systems within the footwall (Andreani et al., 2007; McCaig et al., 2007; Fouquet et al., 2010). In ultramafic and mafic systems, metasomatic assemblages of talc-tremolite-chlorite or quartz form at > 350 °C (Boschi et al., 2006a, 2008; McCaig et al., 2010; Verlaguet et al., 2021), typical of black smoker discharge zones, whereas serpentine-prehnite-hydrogarnet assemblages form at lower temperatures (Frost et al., 2008; Bach and Klein, 2009).

Cores recovered during IODP Expedition 357 have highly heterogeneous rock types, and are variably altered and deformed. Ultramafic rocks are dominated by serpentinized harzburgite with intervals of serpentinized dunite and minor pyroxenite veins; gabbroic layers occur as melt impregnations and veins. Dolerite dikes and basalts are the latest phase of magmatism. Overall, the peridotites show a high degree of serpentinization (> 80 %) and are locally oxidized. In cores with gabbroic intrusions, hydrothermal alteration of mixed peridotite and gabbroic lithologies forms serpentine-talc-amphibole-chlorite assemblages (Boschi et al., 2006b; Picazo et al., 2012).

The petrogenesis of mantle-derived peridotites recovered during IODP Expedition 357 is the subject of this communication. In this paper we use whole rock major, trace and rare earth element (REE) chemistry of Expedition 357 peridotites to discriminate dominant melt-impregnation vs. fluid-dominated processes (i.e., serpentinization, Si metasomatism) and constrain the degrees of partial melting recorded in the peridotites. The altered peridotites are subdivided into Type I serpentinites, Type II melt-impregnated serpentinites and Type III metasomatic serpentinites. Type I serpentinites show no evidence of melt-impregnation or metasomatism apart from serpentinization and local oxidation. Type II serpentinites are distinguishable in some cases on the basis of macroscopic or microscopic evidence and in other cases, are inferred on the basis of incompatible element enrichment in the case of 'cryptically' melt-impregnated serpentinites. Type III serpentinites are characterized by silica metasomatism and the formation of talc-rich alteration assemblages and anomalously high anhydrous SiO_2 concentrations and low MgO/SiO_2 values. In so doing, we geochemically characterize the evolution of mantle lithosphere at a slow-spreading ridge associated with OCC formation, and document spatial compositional variations.

2. Geological setting

The dome-shaped Atlantis Massif OCC is located at 30 °N on the western edge of the MAR axial valley where it intersects the Atlantis Fracture Zone (Fig. 1b). The OCC stretches 15-20 km N–S parallel to the ridge and is 8-12 km wide. Exhumation occurred via low-angle detachment faulting (Cann et al., 1997; Blackman et al., 2002; Schroeder and John, 2004; Karson et al., 2006; Ildefonse et al., 2007). On the basis of its distance from the spreading axis and a calculated spreading half-rate of 12 mm/yr (Zervas et al., 1995), the lithosphere of the massif is considered to be 2.0 to 0.5 Ma (Blackman et al., 2006), a span which encompasses eighteen SHRIMP U/Pb zircon ages of oxide gabbro and felsic dike melt intrusions recovered from Hole U1309D, which range from 1.28 ± 0.05 to 1.08 ± 0.07 Ma (Grimes et al., 2008). Dredging and submersible dives at the massif revealed the dominance of serpentinized peridotite (Blackman et al., 2002; Boschi et al., 2006a; Karson et al., 2006) concentrated primarily along the southern and most elevated portion of the detachment. Samples recovered during IODP Expeditions 304/305, with a drill hole reaching ~ 1500 m depth, consisted almost entirely of olivine-rich mafic intrusive rocks of gabbro and troctolite (Drouin et al., 2009; Ferrando et al., 2018; Godard et al., 2009; Suhr et al., 2008). These geological observations suggest a compositional change of the footwall, with peridotites decreasing in abundance from the segment end towards the north, and also reflecting variations in time of the emplacement of magma in the footwall (Ildefonse et al., 2007).

IODP Expedition 357 cored seventeen shallow holes at nine sites (Fig. 1b) along the detachment fault surface of the Atlantis Massif (Früh-Green et al., 2016). The two eastern sites (M0075, M0068) and one western site (M0071) recovered fault scarp deposits whereas the central sites yielded *in situ* sequences. Most of the sites are aligned along the southern edge of the detachment fault by the Atlantis Fracture Zone wall, with

178 the northernmost hole (M0074) located ~ 6 km north of the detachment's southern edge,
179 and ~ 1 km to the southwest of U1309D. In terms of igneous lithologies and their
180 metamorphosed equivalents, IODP Expedition 357 recovered primarily serpentinized
181 peridotite comprising harzburgite with subordinate dunite (Fig. 1c) and wehrlite with
182 lesser amounts of variably altered mafic inclusions of basalt, gabbro and dolerite (Früh-
183 Green et al., 2018; Rouméjon et al., 2018a; Akizawa et al., 2020). Core lengths range
184 from approximately 1.3 to 16.5 m. Recovery was ~ 75 %.
185
186 **3. Samples and petrography**
187 Except for one talc schist, the protolith of which was mafic, all rocks chosen for
188 study are serpentinized peridotites, and from holes immediately adjacent to the transform
189 fault scarp and drilled at the southern edge of the detachment fault surface (Figs. 1b, c).
190 All peridotites were subjected to high degrees of serpentinization on the order of > 80 %.
191 On the basis of collective macroscopic, microscopic and whole rock chemistry evidence,
192 the studied samples are divided into three types: Type I are serpentinites, Type II are melt-
193 impregnated serpentinites, and Type III are metasomatic serpentinites. Type I
194 serpentinites are ones primarily subjected to serpentinization only, and Types II and III
195 serpentinites have been subjected to mm- to cm-scale mafic melt intrusions and
196 subsequent silica metasomatism, respectively. In the case of melt-impregnation, this is
197 evident in Type II serpentinites by the presence of small veinlets of dolerite (as reported
198 in Expedition 357 petrology logs), and in one case by the presence of rare plagioclase and
199 in another case, by the presence of recrystallized olivine along the peripheries of partially
200 dissolved orthopyroxene (see Fig. 2). Further details regarding evidence for classification
201 of Types II and III are provided in Table 1.

All samples were studied by polarization microscopy. Representative thin section images are given in Figure 2. Sample numbers are taken directly from Früh-Green et al. (2017, Supplementary material). Below, we describe the petrography of each sample type. The mineralogy and mode of the serpentinites are summarized in Table 2.

3.1. Type I serpentinites

Type I serpentinites (Fig. 2a-d) consist of dominant harzburgite (14 of 20 samples) and lesser dunite. Outlines of olivine are generally clear under plane-polarized light (PPL) as serpentinization is most intense around grain boundaries and fractures cutting olivine (e.g., Fig. 2a). Classic mesh-textures are commonly observed. In the harzburgite, orthopyroxene is always altered to bastite, but is nonetheless recognizable under crossed polars by remnant and deformed (curved) cleavage and parallel extinction. Orthopyroxene is typically < 2 mm and olivine is 2-4 mm. Reddish-orange to brown spinel is easily identifiable under PPL and is typically less than 0.5 mm but in some cases up to 4 mm. Spinel occurs both as isolated, angular grains and as subangular and rounded grains commonly arranged in masses or trails of multiple grains. Clinopyroxene was not observed in any samples, reflecting the high degrees of partial melting and melt extraction that many of these peridotites have undergone (see Fig. 3). Modal percentages of the volumetrically dominant harzburgite lie in the range of 75-90 % for olivine and 10-25 % for orthopyroxene; spinel ranges from 0-3 % (Table 2). In the dunite, orthopyroxene is absent and spinel is less common (0 to <1 %) than in the harzburgite.

Four Type I serpentinites exhibit anomalously high CaO contents ranging from 6-13 wt.% (see Table 3). Microscopic inspection reveals that the Ca-rich peridotites exhibit an extensive and densely concentrated, anastomosing network of ~ 0.1 mm thick carbonate veinlets (Fig. 2d).

227

228 *3.2. Type II Melt-impregnated serpentinites*

229 Melt-impregnated serpentinites consist of harzburgite only and comprise six of
230 the 29 studied samples (Table 1). Type II serpentinites in most cases are observed to have
231 mm to cm-scale mafic veins at the scale of drill core (Table 2) although these are not
232 obvious in thin section. Orthopyroxene ranges from ~ 1-5 mm. Modal percentages of
233 olivine and orthopyroxene are 70-90 % and 10-30 %, respectively, with spinel typically
234 absent but reaching 2-3 % in one sample (Table 2).

235 In some Type II serpentinites, other petrographic evidence is present to confirm
236 melt-impregnation. For example, one central harzburgite (76B-7R1-81-83) is the only one
237 in which rare 0.5-0.7 mm plagioclase (< 0.5 % of the mode) is present (Fig. 2e).
238 Plagioclase is highly altered (epidote, sericite) but preserves relict twinning. In another
239 harzburgite from eastern Site M0068B, fresh, 0.5-1 mm olivine constitutes ~ 5 % of the
240 mode, and is observed mantling orthopyroxene (Fig. 2f), which we interpret as replacive
241 following dissolution of orthopyroxene accompanying melt injection.

242

243 *3.3. Type III Metasomatic serpentinites*

244 Type III serpentinites from this study include two harzburgites that are restricted
245 to the eastern sites (Fig. 1c), and are distinguishable on the basis of talc-amphibole
246 alteration of orthopyroxene (Fig. 2e) and whole rock chemistry (see Section 5.1).
247 Orthopyroxene ranges from 1-6 mm. Brown spinel ranges from 0.5-2 mm and are always
248 embedded in orthopyroxene. Modal percentages of olivine and orthopyroxene are ~ 70 %
249 and 30 % respectively, with spinel occupying around 2 % (Table 2).

250

251 **4. Analytical methods and data compilation**

252 *4.1. Whole rock geochemistry*

253 Major and trace element contents of the serpentinites were determined by
254 inductively coupled plasma mass spectrometry (ICP-MS) and atomic emission
255 spectroscopy (ICP-AES) at ALS Geochemistry, North Vancouver, Canada. Prior to
256 shipping to ALS, samples for whole-rock analysis were trimmed to remove weathered
257 surfaces. Samples sent to ALS were crushed to > 70 % passing through a 2 mm mesh,
258 and a 250-g split was pulverized to > 85 % of the material being < 75 μm in diameter.
259 Powders were then analyzed for whole rock major and trace element determinations. For
260 major element oxides, 100 mg of powered sample was added to lithium
261 metaborate/lithium tetraborate flux, mixed well and fused in a furnace at 1000 °C. The
262 resulting melt was dissolved in 100 mL of 4 % HNO_3/2 % HCl. This solution was then
263 analyzed by ICP-AES (ALS Geochemistry method ME-ICP06) and the results were
264 corrected for spectral inter-element interferences. Major element detection limits are
265 0.01% for all oxides except Cr_2O_3, which is 0.002 % (Supplementary Table S1). For loss
266 on ignition (LOI), 1 g of sample powder was heated at 1000° C for one hour, cooled and
267 then reweighed, with percent LOI calculated by the difference in weight.

268 For trace and rare earth elements, the ME-MS61L Super Trace and MS61L-REE
269 methods (https://www.alsglobal.com/) were employed, which combines a four-acid
270 digestion with ICP-MS instrumentation utilizing collision/reaction cell technologies to
271 provide the lowest detection limits available. In the first method, analyzed elements
272 include Ba, Cd, Ce, Co, Cr, Cs, Cu, Ga, Hf, La, Li, Mo, Nb, Ni, Pb, Rb, Sc, Sn, Sr, Ta,
273 Te, Th, U, V, W, Zn and Zr; in the second method, analyzed elements include Dy, Er, Eu,
274 Gd, Ho, Lu, Nd, Pr, Sm, Tb, Tm and Yb. This trace method has been optimized for long-
275 term robust ICP-MS signal stability, in particular for samples with high Ca content. The
276 prepared samples (nominal weight 0.25 g) were digested with 1.5 mL concentrated HNO_3

277 and $HClO_4$, followed by concentrated HF. Subsequently, the mixture was heated at 185
278 °C until incipient dryness, leached with 50 % HCl and diluted with weak HCl. The final
279 solution was then analyzed by ICP-MS with results corrected for spectral inter-element
280 interferences. Apart from Ba, Cr, Sn, V, W and Zr with detection limits that range from
281 0.3-5 µg/g, detection limits of the remaining trace elements ranged from 0.001-0.2 µg/g
282 (Supplementary Table S1).

283 Results of duplicate analyses and analytical standards used are provided in
284 Supplementary Table S2. Reproducibility of these reference samples is generally better
285 than 5 % for concentrations more than 10 x above the detection limit, and typically 5-20
286 % closer to the detection limit.

287

288 *4.2. Data compilation*

289 The stratigraphic location of samples analyzed for whole rock chemistry in this
290 study are shown in Fig. 1c. The new whole rock geochemical data of 29 whole rock ICP-
291 MS and ICP-AES geochemical analyses from this study (Table 3) are compared with the
292 ten Expedition 357 peridotite samples of Früh-Green et al. (2018) and the four Atlantis
293 Massif peridotite samples of Godard et al. (2009) from Site 1309 in Figs. 3-10. We also
294 compare these data with whole rock geochemical data compiled from global abyssal
295 peridotites of Niu (2004), Paulick et al. (2006), and Godard et al. (2008).

296

297 **5. Results**

298

299 *5.1. Whole rock chemistry major elements and Ni and Cr abundances*

300 In MgO/SiO_2 vs. Al_2O_3/SiO_2 space (Fig. 3) the 'terrestrial array' represents the
301 successive magmatic depletion (or melt extraction) trend of primitive mantle. Highly
302 depleted compositions are characterized by low Al_2O_3/SiO_2 of < 0.01 (Jagoutz et al.,

303 1979; Hart and Zindler, 1986). Verification of this melt extraction trend is reflected by a
304 global data set of MOR peridotites (compilation of Niu, 2004; Paulick et al., 2006; Godard
305 et al., 2008). Atlantis Massif serpentinized harzburgites record Al_2O_3/SiO_2 that range
306 from ~ 0.01-0.04 indicating moderate to high degrees of magmatic depletion. Two Type
307 I serpentinized dunites from the central sites (M0076B-3R1-78-82, M0076B-5R1-59-61,
308 Table 1), and one dunite (1309D-31R-25-28) from Site U1309 reported by Godard et al.
309 (2009) exhibit $Al_2O_3/SiO_2 < 0.01$. Very low Al_2O_3/SiO_2 values can alternatively be
310 caused by replacive melt-rock interaction. Vertical deviations from the terrestrial array
311 are indicative of Mg-Si mass transfer; peridotites that exhibit MgO/SiO_2 below the
312 terrestrial array may reflect magnesium loss or silica addition during serpentinization or
313 magnesium loss during seafloor weathering (Snow and Dick, 1995; Niu, 2004). A trend
314 defined by increasing Al_2O_3/SiO_2 with most samples offset to moderately low MgO/SiO_2,
315 as seen in the Atlantis Massif serpentinites (Fig. 3), can also be partially attributed to
316 melt-impregnation processes (Niu, 2004). Half of the eight Type II melt-impregnated
317 serpentinites of the eastern and central sites from this study and the study of Früh-Green
318 et al. (2018) exhibit MgO/SiO_2 of < 0.9, consistent with this process; nonetheless, all
319 melt-impregnated serpentinites plot within the range of the Type I serpentinites. Two
320 central serpentinites yield MgO/SiO_2 values of ~ 0.76-0.86, within the lower range of the
321 melt-impregnated serpentinites, which suggests that these two samples may also have
322 been subjected to processes associated with melt-impregnation. Silica-metasomatism is
323 characterized by low MgO/SiO_2 (< 0.55) and low Al_2O_3/SiO_2 (< 0.025). One exception
324 is the talc schist, which exhibits low MgO/SiO_2 (~ 0.4) but high Al_2O_3/SiO_2 of 0.11, which
325 suggests the addition of silicic melt (Paulick et al., 2006).

326 In Fig. 4 we plot MgO vs. selected major element oxides and loss on ignition
327 (LOI) to illustrate the effects of serpentinization and multiphase alteration processes on

major element chemistry. In terms of MgO and other major element oxides, the Type I serpentinites generally plot similarly to global MOR peridotites. Apart from two serpentinized harzburgites, which exhibit anomalously high Al_2O_3 and CaO, the remaining serpentinites have MgO contents that ranges from 41.25 to 46.06 wt.% and Mg# ($Mg/Mg+Fe^{2+}$) of 87.6-91.8 (Table 3). In SiO_2 vs. MgO space (Fig. 4a) the serpentinites and melt-impregnated serpentinites fall almost completely within the range of global abyssal peridotite and plot similarly to, but with slightly lower SiO_2 contents than the bulk composition of serpentine. In contrast, the Type III talc-altered serpentinites and talc schists plot near the bulk composition of talc and ODP Leg 209 talc-altered peridotites, but with slightly lower SiO_2 and MgO. The Ca-rich Type I serpentinites (6.66-13.30 wt.% CaO) plot off the linear array of the serpentinites and melt-impregnated peridotites in SiO_2 vs. MgO space with significantly lower SiO_2 at similar MgO. Fe_2O_3, Al_2O_3 and CaO contents (Figs. 4b-d) of the talc-altered serpentinites and talc schists generally fall within the range of the Type I and II serpentinites. Apart from two Type II melt-impregnated serpentinized harzburgites, which exhibit slightly higher Al_2O_3 contents than the remaining serpentinites, other major element oxide concentrations of the melt-impregnated serpentinites are similar to those of the serpentinites. CaO contents in the western site Type I serpentinites (Fig. 4d) record lower concentrations (0.05-0.30 wt.%) than those of the central and eastern sites. Similar to the SiO_2 vs. MgO plot, significant differences exist in LOI values between the Ca-rich serpentinites and all other serpentinites (Fig. 4e). Whereas the bulk of the peridotites exhibit LOI of ~ 12-14 wt.%, similar to those of global MOR peridotites and the talc-altered harzburgites and schists have low LOI contents that range from ~ 4-6 wt.%, similar to ODP Leg 209 talc-altered peridotites, the Ca-rich serpentinites have high LOI of ~ 16-20 wt.%. The Type II melt-

352 impregnated serpentinites have LOI values that are up to ~ 9 wt.%, intermediate between
353 those of the Type I and serpentinites and Type III serpentinites and schists.
354 The majority of the Expedition 357 serpentinites have Ni and Cr concentrations
355 of ~ 1000-3000 µg/g (Table 3), similar to that of primitive mantle (PM), and fall within
356 the range of global MOR peridotites (Supplementary Fig. S1). Exceptions are two central
357 and two western serpentinite samples from Früh-Green et al. (2018), which range to Ni >
358 10000 µg/g and Cr > 30000 µg/g, and two central serpentinized dunites and two eastern
359 melt-impregnated harzburgites from our study, which exhibit low Cr (< 400 µg/g).
360
361 *5.2. Whole rock trace element concentrations*
362 Significant differences in the relative degree of depletion, pattern morphology,
363 and the existence of prominent element anomalies, e.g., conspicuous positive or Ce-
364 anomalies depending on serpentinite type, are apparent on the basis of chondrite-
365 normalized REE and PM-normalized incompatible trace element patterns (Fig. 5).
366 Patterns range from those similar to and significantly more depleted than depleted MORB
367 mantle (DMM) and mean abyssal peridotite in western Site M0071, central Sites M0069
368 and M0076, and Atlantis Massif IODP Site U1309 (Godard et al., 2009) to patterns
369 enriched relative to DMM and mean abyssal peridotite as shown by central Site M0072
370 and most of eastern Site M0068. The serpentinites from eastern Site M0068 are atypical
371 to other Expedition 357 serpentinites in that they exhibit LREE enrichments but HREE
372 concentrations intermediate to that of DMM and mean abyssal peridotite. Central Site
373 M0072 and eastern Site M0068 serpentinites typically exhibit REE concentrations that
374 are more enriched than DMM and range from ~ 1-10 x chondrite; two M0068 talc schists
375 are exhibit high REE concentrations of ~ 20 x chondrite.

376 Type I serpentinites sampled at western Site M0071, and central Sites M0069 and
377 M0076 exhibit low Yb as well as low abundances of other incompatible elements, for
378 example the high-field strength elements (HFSE) Nb and Zr (Table 3). Apart from one
379 central Site M0072 serpentinized dunite with similarly low Yb, Nb and Zr, the remaining
380 central Site M0072 and eastern site serpentinites, many of which are Type II melt-
381 impregnated or Type III metasomatic serpentinites, exhibit comparatively higher
382 concentrations of these incompatible elements (Table 1). As we show in Section 6.2.3,
383 the melt-impregnated serpentinites, in particular in central Site M0072 and eastern Site
384 M0068, show high concentrations of most incompatible elements relative to other sites.
385 Although the highly depleted Type I serpentinites from the western and central
386 sites exhibit mostly concave upwards REE patterns with a steady decrease in REE
387 abundances from the HREE to LREE, central Site M0072 Type I and Type II serpentinites
388 exhibit flatter patterns; the eastern Types I, II and III serpentinites are atypical relative to
389 the serpentinites to the west (i.e., at the central and western sites) in that they exhibit
390 LREE enrichment. Excluding the lone, Ca-rich (12.46 wt.% CaO) serpentinized dunite
391 with La/Sm_{CN} (CN denotes chondrite-normalized) of 4.70 and La/Yb_{CN} of 2.39, the
392 western Type I serpentinites from Site M0071 exhibit mostly moderate but variable
393 LREE/MREE fractionation (La/Sm_{CN} of 0.40-3.03) with La/Yb_{CN} ranging from 0.11-
394 0.68. In contrast, the two eastern Type I serpentinites exhibit relatively minor LREE
395 enrichment with La/Sm_{CN} and La/Yb_{CN} ranging from 1.08-1.17 and 1.13-1.30,
396 respectively; the eastern Type II melt-impregnated serpentinites have higher LREE
397 enrichments with La/Sm_{CN} = 1.72-2.15 and La/Yb_{CN} = 1.43-1.68 and the Type III
398 metasomatic serpentinites have $LaSm_{CN}$ = 0.41-1.41 and La/Yb_{CN} = 0.48-1.36.
399
400 **6. Discussion**

401 On the basis of trace and rare earth element chemistry, we address differences in
402 the compositions of the different serpentinite types to discriminate dominant fluid-rock
403 interaction processes associated with serpentinization, from processes associated with
404 mafic melt-rock interaction. We then provide estimates of degrees of partial melting (melt
405 extraction) recorded in serpentinites sampled across the Atlantis Massif (IODP Exp. 357),
406 before linking the geochemistry to processes associated with oceanic core complex
407 formation.
408
409 *6.1. Evidence of fluid-dominated serpentinization processes*
410 Significant observations from the chondrite-normalized REE and PM-normalized
411 patterns are: (1) prominent negative Ce-anomalies (i.e., Ce/Ce* where Ce* =
412 $\sqrt{(La_{CN}*Pr_{CN})}$ and $Ce = Ce_{CN}$) in the western Type I serpentinites and two central Type I
413 serpentinites, and positive Ce-anomalies in almost all eastern serpentinites (the vast
414 majority of other central serpentinites show Ce/Ce* ~ 1); (2) extreme U-enrichment in
415 many serpentinites with values that range to nearly 300 x PM; and (3) extreme Sr-
416 anomalies with enrichments of up 100 x PM in most Ca-rich Type I serpentinites and
417 depletion to below 0.1 x PM in the serpentinites of Sites M0072 and M0068.
418 With respect to the negative Ce-anomalies exhibited mostly by the western Type
419 I serpentinites (site M0071), such anomalies in peridotites have been attributed to
420 seawater-peridotite interaction (e.g., Frisby et al., 2016a, b) and indeed, (oxygenated)
421 seawater itself exhibits a negative Ce-anomaly (e.g., Elderfield and Greaves, 1982).
422 The western site Type I serpentinites range to the highest U concentrations (5.05
423 µg/g), whereas the Type II melt-impregnated serpentinites of central site M0072 and
424 eastern site M0068 range to the lowest U concentrations (0.01 µg/g) (Fig. 6a, Table 3),
425 which suggests that U enrichment is associated with serpentinization and oxidation, and

not melt-impregnation. Uranium enrichment in serpentinites is common as U is hosted by serpentine phases (e.g., Deschamps et al., 2010). Frisby et al. (2016a, b) have shown that U enrichments correlate with Ce anomalies and the amount of Nd derived from seawater, which is a proxy for water/rock values. Thus, U enrichments have been shown explicitly to reflect fluid-rock interaction in abyssal peridotites.

In the case of Sr enrichment (Fig. 6b), evidence is not as clear. However, we note that the Type II melt-impregnated central site M0072 and eastern site M0068 serpentinites range to the lowest Sr concentrations, with the former exhibiting the lowest concentrations of Sr (1.02-4.01 μg/g) of all sites, whereas the other sites locally show distinct Sr enrichments. This suggests that Sr enrichment is not associated with melt-impregnation.

6.2. Evidence for melt-impregnation processes: Enrichment in incompatible elements, LREE, LREE fractionations and ΣREE

As explained above, we infer melt-impregnation in central site M0072 serpentinites on the basis of compositional similarities with melt-impregnated serpentinites constrained on the basis of macroscopic and microscopic evidence, even though site M0072 serpentinites lack observable evidence of melt-impregnation at the scale of core and thin section. Hence, due to the absence of such mineralogical evidence, we term these M0072 serpentinites 'cryptically melt-impregnated'.

The HFSE, e.g., Th, Hf, Zr (Figs. 7a-c), Nb, and Ti are highest in Type II melt-impregnated serpentinites at central Site M0072 and eastern Site M0068 and lowest in western sites Type I serpentinites. In addition, Figures 7d and 7e show an increase in LREE and ΣREE, and possibly LREE fractionation from Type I serpentinites to Types II and III serpentinites, and from west to central to east. For example, apart from a lone Ca-

rich Type I serpentinized dunite, which exhibits anomalously high La and anomalously low Ce and La/Yb_{CN} of 2.39, the remaining western Type I serpentinites yield La/Yb_{CN} of 0.11-0.47 and mean ΣREE of 0.39 µg/g (including the Ca-rich dunite). The central Type I and II serpentinites yield a range of La/Yb_{CN} of 0.15-1.31 and mean ΣREE of 2.40 µg/g, and the eastern Types I, II and III serpentinites yield a range of La/Yb_{CN} of 0.61-1.68 and mean ΣREE of 12.66 µg/g. Thus, overall, melt impregnation produces less LREE fractionation and more elevated ΣREE compared to processes dominated by fluid-rock interaction.

6.3. Evidence of silica metasomatism

Talc- and amphibole-rich fault rocks form as the result of silica metasomatism and have been recovered from detachment fault surfaces along slow and ultra-slow spreading mid-ocean ridges including oceanic core complexes (e.g., Escartín et al., 2003; Schroeder and John, 2004; Boschi et al., 2006b; McCaig et al., 2007; Picazo et al., 2021). These rocks record heterogeneous deformation under greenschist-facies conditions and are commonly restricted to localized shear zones (< 200 m), which are associated with intense talc-amphibole metasomatism (Escartín et al., 2003; Boschi et al., 2006b). Talc is mechanically weak and thus may be critical to the development of such fault zones and may enhance unroofing of upper mantle peridotites and lower crustal gabbroic rocks during seafloor spreading. In the case of the Atlantis Massif, talc metasomatism is associated with serpentinite dehydration (Boschi et al., 2008). Strontium isotope compositions of talc-rich fault rocks indicate that talc metasomatism along detachment faults occurs at low water/rock values (0.2–0.7) and reflect interaction with Si-rich, evolved fluids with a mafic component derived from interaction with gabbro lenses within a peridotite-dominated ridge segment (Boschi et al., 2008).

In our study, silica metasomatism is reflected by plots of MgO/SiO_2 vs. Al_2O_3/SiO_2 (Fig. 3) and MgO vs. SiO_2 (Fig. 4a). These figures demonstrate the distinct whole rock geochemistry of the talc-altered Type III metasomatic serpentinites and talc schists from the eastern site M0068. In MgO vs. SiO_2 space (Fig. 4a), the talc-bearing serpentinites and talc schists are clearly distinct from all other Exp. 357 serpentinites by much lower MgO and much higher SiO_2 contents. These low MgO/SiO_2 and Al_2O_3/SiO_2 values of < 0.02 are indicative of silica metasomatism and are close to compositions of talc-bearing harzburgites recovered during ODP Leg 209 (Paulick et al., 2006).

6.4. Discrimination of fluid-rock vs. melt-dominated processes

6.4.1. Comparison with global abyssal peridotites

Figure 8a highlights trace element variations of mean global abyssal peridotites with compositions dominated by melt-rock interaction vs. those dominated by fluid-rock interaction associated with serpentinization (as interpreted by Paulick et al., 2006). We note that (in Fig. 8) we are comparing patterns, as absolute concentrations are subject to other processes (e.g., melt addition). Serpentinites subjected to mafic melt-impregnation exhibit enrichments in incompatible elements relative to those that have not been affected by melt-impregnation (Fig. 8a). In Figure 8b, we plot the mean serpentinite composition of each Expedition 357 location (i.e., west, central, east) vs. the mean compositions of melt-dominated and fluid-dominated global abyssal peridotites as shown in Fig. 8a. In Fig. 8c, we parse the mean peridotite compositions according to borehole of the central sites. There are clear differences in incompatible element concentrations between Exp. 357 Type II melt-impregnated serpentinites and Type III metasomatic serpentinites relative to Type I serpentinites, with Types II and III exhibiting greater abundances of all incompatible elements (Fig. 8b). In particular, the Type I serpentinites from the western

site have PM-normalized incompatible element abundances that are most similar to fluid-dominated peridotites, whereas central sites serpentinites exhibit concentrations most similar to melt-dominated peridotites; eastern site serpentinites have incompatible abundances more enriched than melt-rock dominated peridotites (Fig. 8b). Apart from U and Sr, the Exp. 357 serpentinites show a clear enrichment in all other incompatible elements from the western to central to eastern sites (Fig. 8b).

6.4.2. HFSE vs. LREE

On the basis of selected HFSE vs. LREE and HFSE vs. MREE/HREE variations, Paulick et al. (2006) showed that the global abyssal peridotite dataset of Niu (2004) exhibit relatively steep positive trends, which was interpreted as indicative of dominant melt-rock interaction processes. The reason for this trend is related to differences in the behavior of LREE and HFSE; LREE are more hydrophilic than HFSE, and so are more readily transported in solution. Although melt-rock reaction mobilizes both LREE and HFSE, fluid-dominated reactions preferentially mobilize LREE, resulting in distinctly different patterns (Niu, 2004). A trend defined by only minor increase in HFSE concentrations (i.e., a sub-horizontal as opposed to steep positive trend) on the other hand, is indicative of dominantly hydrothermal alteration processes (i.e., fluid-rock interaction), which affect the more immobile HFSE to a lesser extent than the REE (Paulick et al., 2006). In the dataset of ODP Leg 209 peridotites, Paulick et al. (2006) showed that those at Sites 1270 and 1271 exhibit steep trends similar to the dataset of Niu (2004), whereas those of Sites 1268, 1272 and 1274 show less steep, subhorizontal trends, which they interpreted as more consistent with fluid-rock interaction.

Fig. 9 shows Expedition 357 serpentinites vs. the trends of global abyssal peridotites, with compositions dominated by (i) melt-rock interaction, and (ii) fluid-rock

interaction in Nb vs. La and Ti vs. Dy space. These plots produce two distinct linear trends, which mimic the two described above, in agreement with the observations presented in Fig. 8. The serpentinites of the central and eastern sites, which show ample evidence of melt-impregnation, exhibit steep trends indicative of compositions dominantly controlled by melt-rock interaction similar to those of the global MOR peridotite dataset of Niu (2004) and ODP Leg 209 Sites 1270 and 1271 of Paulick et al. (2006). In contrast, Type I serpentinites from the western site, which show minimal evidence of melt-impregnation, instead show flatter, subhorizontal trends suggestive of compositions mostly controlled by fluid-rock reactions, similar to trends of peridotites of ODP Leg 209 Sites 1268, 1272 and 1274. We note also that similar relations and trends occur on other plots of HFSE vs. LREE and MREE (e.g., Th vs. Ce, Ti v. Ce, Hf vs. Pr, Nb vs. $[Gd/Lu]_{CN}$ and Ti vs. $[Gd/Lu]_{CN}$, Supplementary Fig. S2). In the case of Expedition 357 serpentinites, in all instances, the slope of the trends of the central and eastern site serpentinites are steeper than the slope of the trend of the western site serpentinites, consistent with compositions of the former being the result of dominant melt-rock reaction and compositions of the latter being the result of dominantly fluid-rock interaction. When the central location is parsed into discrete sites, compositions of serpentinites from central Site M0069 are consistent with being dominated by fluid-rock interaction, whereas those of central Sites M0072 and M0076 are consistent with being dominated by melt-rock interaction.

6.5. Petrogenesis: Estimates of degrees of melt extraction

Chondrite-normalized REE and PM-normalized patterns (Fig. 5) are used to explain differences in the relative depletion of peridotites of each site investigated and provide evidence of fluid-dominated processes and melt-impregnation processes

551 (Sections 6.1.-6.4.), based on the compositional variation of Expedition 357 serpentinites.
552 Below, we model estimates of partial melting undergone by the peridotites based on trace
553 and REE chemistry.

554 Various highly incompatible and immobile trace elements (Yb, Nb, Zr) in
555 serpentinites from western Site M0071 and central Sites M0069 and M0076 exhibit
556 extreme depletion relative to DMM, in contrast to the central Site M0072 serpentinites
557 that exhibit enriched chondrite-normalized patterns relative to DMM apart from a lone
558 moderately depleted Type I serpentinized dunite. The eastern Site M0068 serpentinites
559 exhibit LREE concentrations more enriched than DMM but HREE slightly to moderately
560 more depleted than DMM. Evidence in support of high degrees of melt depletion includes
561 the high depletion in Al_2O_3 and CaO (Fig. 4), and the aforementioned other incompatible
562 trace elements (Fig. 7, Table 3). Below, we provide estimates of the maximum degrees of
563 melt extraction based on modelling of whole rock REE concentrations and note that REE
564 patterns of many samples are strongly affected by refertilization, which thus needs to be
565 taken into account to derive accurate estimates of melt depletion.

566 The REE patterns of the most melt-depleted sample for each of the five sites are
567 shown in Fig. 10 and compared with curves predicted by modeling of melt depletion
568 followed by subsequent metasomatism. As LREE are most strongly depleted during
569 partial melting, and therefore sensitive to refertilization, this part of the REE pattern is
570 essentially that of the metasomatizing agent. As a result, different amounts of
571 metasomatism will shift the LREE pattern up or down, but the slope of the LREE pattern
572 (La/Sm) is barely affected. This slope is strongly variable in our dataset, ranging from
573 LREE-depleted ($[La/Sm]_{CN}$ = 0.3-0.9) to strongly enriched ($[La/Sm]_{CN}$ = 2-5). The REE
574 patterns in Figs. 5a-e show at least two distinct melts that have infiltrated the peridotites,
575 an enriched (*E*) and a depleted type (*D*), of which the most REE-rich examples are from

576 eastern Site M0068 (samples 68A-1R1-34-35 and 68A-1R1-1-6). In these samples, the
577 original peridotite REE patterns have been completely overprinted by the infiltrating
578 melts. Therefore, we chose these peridotites to estimate the composition of the two
579 endmember contaminants during modeling (*E* and *D*, respectively). Both types can be
580 observed at each site, although central Sites M0072 and M0076 are dominated by a *D*-
581 type contaminant. Some serpentinites show evidence of infiltration by an even more
582 enriched contaminant (*SE*), the composition of which is more difficult to estimate. As this
583 contaminant is strongly LREE-enriched and therefore relatively HREE poor, its exact
584 composition will have little effect on our melt fraction estimates, which are based on the
585 HREE part of the patterns.

586 The calculated volume of fractional non-modal melt extraction (see Fig. 10
587 caption for model parameters) of the most depleted sample from each site ranges from 19
588 to 21 % (Fig. 10), which indicates little difference in the maximum amount of melt
589 extraction between the sites. The difference in the REE patterns between the sites are
590 primarily due to small but variable amounts of infiltrating melts (<1 % for each of the
591 five most depleted samples, Fig. 10).

592 These modeling results show little difference in the maximum amount of melt
593 extraction between the different sites across the footwall. Unfortunately, significant melt
594 infiltration experienced by many of the serpentinites makes it difficult to evaluate the
595 average amount of melt extraction experienced by serpentinites of the different sites. For
596 example, nearly all whole rock compositions of eastern Site M0068 and central Site
597 M0072 are more enriched than DMM, which could be interpreted as very limited melt
598 extraction, but refertilization of these samples will have obliterated any previous melt
599 extraction history. Our modeling results suggest that differences in REE patterns observed
600 between sites are probably due to differences in refertilization, not partial melting.

601

602 *6.6. Spatial variations in geochemical processes and peridotite composition*

603 It was noted by Früh-Green et al. (2018) that there exists a weakly defined
604 enrichment in peridotites from west to east. This pattern is actually strongly defined in
605 terms of enrichment in LREE, LREE fractionation, ΣREE, and HFSE (Figs. 7-9 and
606 Supplementary Fig. S2). For example, Fig. 8 shows a distinct increase in all incompatible
607 elements except U, Pb, and Sr in the mean serpentinite compositions moving from west
608 to central to east. Specifically, the western Type I serpentinites exhibit the lowest
609 concentrations of HFSE of Nb, Zr, and Th whereas the eastern serpentinites exhibit the
610 highest concentrations of these elements (Figs. 7a-c); the central serpentinites have
611 concentrations intermediate to the western and eastern serpentinites. However, as we have
612 also noted, there are distinctions in the central location when parsed into individual sites
613 with central Site M0069 being depleted to the same degree as the western serpentinites
614 and with the two other central sites (M0072 and M0076) being comparatively more
615 enriched.

616 Moreover, this pattern of west to east enrichment is complementary to the relative
617 volume of melt-impregnation and silica metasomatism recorded in sampled peridotite at
618 each site. The eastern site comprises the largest percentage of melt-impregnated and
619 silica-metasomatized peridotites (70%), relative to the central sites (35%), and the
620 western site (a single sample out of nine, or 11%, is melt-impregnated, with no Type III
621 silica-metasomatized serpentinites). However, the calculation for the central sites is
622 underestimated as we do not include here the four cryptically melt-impregnated
623 serpentinites of central Site M0072 from our dataset, which show no macroscopic or
624 microscopic evidence of melt-impregnation. If we recalculate with the inclusion of these

four M0072 serpentinites, the percentage of melt-impregnated and silica-metasomatized peridotites from the central sites increases to 52 %.

6.7. Links to OCC processes

The observed spatial variations in serpentinite composition needs to be interpreted in the context of both the limitations of our observations and taking into account the complex history of detachment fault formation and exhumation. We have shown that the western site Type I serpentinites record compositions consistent with dominantly fluid-rock interaction processes, whereas the central site serpentinites, considered collectively, and those from the eastern site record compositions consistent with having undergone dominant melt-rock interaction. Furthermore, there is a clear progression in the volume of melt-impregnations from west to central and east and a corresponding increase in incompatible element enrichment, a record of these increasing volumes of melt-enrichment.

Serpentinites from the western sites originated from shallower borehole depths of ~ 0-10 m relative to those of the central sites (a maximum of ~ 16 m in the cases of central Sites M00069A and M0076A, Fig. 1c). The present-day position of these samples cannot be directly related to that of the history of each sample, from lithospheric emplacement, subsequent interaction with melt, alteration, and exhumation. First, the detachment fault zone is likely a complex, anastomosing structure, with a thickness of ~100 m to ~ a few 100s of m (e.g., Karson et al., 2006; Escartín et al., 2017; Parnell-Turner et al., 2018), where fault blocks are transposed in the across-axis direction. In this case, variations in composition vs. borehole depth may not correspond to actual structural depths relative to the fault surface exposed at the seafloor, and now adjacent materials may have originated from different positions in the deformed fault zone. Second, the boreholes also include

650 talus material that is therefore not *in situ*. The present-day location of these samples
651 cannot be directly interpreted as an indicator of spatial and temporal relationships with
652 samples *in situ*, and therefore have an ambiguous structural position. If these debris fields
653 correspond to local mass-wasting deposits, visible at small scales over the detachment
654 fault, the present-day position may be close to the original *in situ* position. Oceanic
655 detachments also display a cover of rubble and sediment that is sourced from the hanging
656 wall, and rafted during extension (e.g., Dick et al., 2008; Escartín et al., 2017). Thus, if
657 the talus material corresponds to rubble cover, its source may be the hanging wall rather
658 than the fault zone or footwall instead, and its present-day location does not necessarily
659 reflect its position at the time of formation, emplacement, impregnation, or alteration.
660 The consistent grouping of samples with a similar melt-impregnation (or lack
661 thereof) and alteration history at the eastern, central, and western sites may suggest that
662 *in situ* samples have not witnessed significant (km-scale), lateral transposition along the
663 fault zone, or at least at spatial scales that are smaller than any local spatial variation
664 associated with melt-rock interactions. Similarly, the samples that are not *in situ*, with
665 similar melt impregnation and alteration histories, suggest a local source; sampling of
666 hanging wall rubble would likely result in an extremely heterogeneous and variable set
667 of ultramafic samples, as observed from the rubble cover from other oceanic detachments
668 (e.g., Escartín et al., 2007). The homogeneity is therefore consistent with a local origin,
669 with material sourced from the mass-wasted fault zone, eventually mixed with basaltic
670 rubble that is present in the boreholes (e.g., Früh-Green et al., 2018).
671 If the samples were either *in situ*, or sourced locally where *ex situ*, and if the lateral
672 transposition of material within an anastomosing fault zone occurs at a smaller scale (< 1
673 km parallel to extension) than the distance between sites (3-5 km), then spatial patterns
674 observed may be interpreted in the context of the internal structure and evolution of the

675 OCC and its detachment fault. Ildefonse et al. (2007) suggested a temporal variation in
676 melt supply to the ridge axis, with an initial phase of accretion that has limited melt
677 supply, and a late phase of accretion with increased melt supply and the emplacement of
678 gabbros in the footwall. This interpretation is consistent with early peridotites just
679 showing melt extraction (western sites), and melt-rock reactions in more recent time
680 associated with this recent magmatic phase (eastern sites).

681 Alternatively, the sites may simply record an inherently heterogeneous system,
682 where melt percolation, and hence melt-rock reactions, are inherently inhomogeneous. If
683 this is the case, the east-west patterns may not reflect a temporal evolution but instead
684 indicate that these heterogeneities occur over distances of a few km, corresponding to the
685 separation among the different sites. This interpretation is consistent with geological
686 observations and drilling that document a change in footwall composition along-axis,
687 with peridotites near the transform fault wall, and gabbros ~ 10 km to the north, hence at
688 spatial scales similar to those shown by the western, central, and eastern sites.

689

690 **7. Conclusions**

691 Peridotites sampled during IODP Expedition 357 comprise predominantly Type I
692 serpentinites, with lesser Type II melt-impregnated and Type III metasomatic
693 serpentinites. A principal variation in the nature and composition of Expedition 357
694 serpentinites is an increase in the volume of melt-impregnation products and a
695 concomitant increase in HFSE and LREE enrichments from the western to central to
696 eastern sites. Whole rock chemical compositions of western site Type I serpentinites are
697 consistent with dominantly fluid-rock interaction associated with serpentinization and
698 oxidation, whereas compositions of eastern site Type II melt-impregnated and Type III
699 metasomatic serpentinites are dominated by melt-rock interaction processes. High to

700 moderate degrees of melt extraction in the peridotites are evident in low concentrations
701 of Al_2O_3, CaO and incompatible elements. Degrees of melt extraction based on whole
702 rock REE suggest a high range of 19-21 % with no apparent variation between sites. Some
703 serpentinite samples are rubble and therefore *ex situ*. Thus, the coherent magmatic history
704 observed at each site may be consistent with a local source originating in the fault zone
705 rather than rafted rubble that would be expected to show more heterogeneity and no
706 spatial pattern. If this is accurate, our sites may provide a time-record of enhanced melt-
707 rock interaction with time, consistent with proposed geological models. Otherwise, the
708 magmatic history may represent heterogeneities in these processes at spatial scales of a
709 few km.
710

711 **Acknowledgments**

712 *This research used samples and data provided by the International Ocean Discovery*
713 *Program (IODP). This project would not have been possible without the support of the*
714 *entire IODP Expedition 357 scientific party and support staff from the ECORD Science*
715 *Operator. In particular, we thank co-Chief Scientist Beth Orcutt, Expedition Project*
716 *Managers Carol Cotterill and Sophie Green, Offshore Operations Manager David Smith,*
717 *the ESO Laboratory and Curation Manager Ursula Roehl, and the entire team of the*
718 *Bremen Core Repository at MARUM. Funding for Expedition 357 was provided by the*
719 *European Consortium for Ocean Research Drilling (ECORD). SAW acknowledges*
720 *financial support from the Korea International Ocean Discovery Program (K-IODP)*
721 *funded by the Ministry of Oceans and Fisheries, Korea and internal funds provided by*
722 *KFUPM Dept. of Geosciences. GFG acknowledges funding by the Swiss National Science*
723 *Foundation (SNF) project No. 200021_163187 and Swiss IODP. MIL acknowledges that*
724 *this research was undertaken thanks in part to funding from the Canada First Research*

Excellence Fund through the Arthur B. McDonald Canadian Astroparticle Physics Research Institute.

Figure captions

Figure 1. (a) Location of the Atlantis Massif at 30°N within the context of the greater MAR spreading system (modified from Kelley et al., 2001). (b) Bathymetric map centered on the southern wall of the Atlantis Massif (modified after Rouméjon et al., 2018a). Inset shows the location of the Atlantis Massif on the western flank of the Mid-Atlantic Ridge axial valley, bordered to the south by the Atlantis Fracture Zone. Circles with numbers in italics and beginning with M00 represent shallow drill hole locations from IODP Exp. 357 (Früh-Green et al., 2017, 2018). White circles indicate drill holes with no recovered peridotite; blue, red and yellow circles represent western (M0071), central (M0069, M0072, M0076) and eastern (M0068) sites, with recovered peridotite samples investigated in this study. White squares represent sites (U1309, U1310, U1311) drilled during Exp. 304/305 (Blackman et al., 2006); white star shows the location of the Lost City Hydrothermal Field (LCHF) (Kelley et al., 2001). (c) Simplified downhole plots showing dominant rock types recovered in the seven drill holes hosting serpentinized peridotites (modified from Roumejon et al., 2018a; see Fruh-Green et al., 2018 for complete expedition drill hole vertical sections). The sections are arranged from right to left according to longitude (see Fig. 1b), and from hole top to bottom. The central holes embody *in situ* segments of the detachment footwall, whereas the western and eastern site holes which yield rubbly intervals and sedimentary structures are interpreted as artefacts of mass wasting and local faulting. Symbols: circles, harzburgite; squares, dunite; triangles, Ca-rich harzburgite; triangles with slash, Ca-rich dunite; crosses, melt-impregnated harzburgite; x's, plagioclase-impregnated harzburgite; diamonds, talc-

amphibole altered harzburgite; diamonds with slash; talc-amphibole-chlorite schist. Blue, red and yellow symbols represent samples of western, central and eastern serpentinized harzburgites and dunites, respectively, analyzed for whole rock chemical analysis. Note 'metamafic' includes metabasalt, metadolerite and metagabbro composition samples.

Figure 2. Representative thin section images of Expedition 357 Type I serpentinites (a-d), Type II (mafic) melt-impregnated (mm-i) serpentinite (e, f) and Type III metasomatic serpentinites (msp) (g, h). 'Typical' completely serpentinized peridotite samples from (a, b) 71A-1R2-85-89, harzburgite and (c) 71C-5R1-6-8, harzburgite. (d) Ca-rich serpentinized harzburgite 69A-9R2-8-12 showing extensive network of carbonate veinlets. (e, f) Mafic melt-impregnated (mm-i) harzburgites 76B-7R1-81-83 and 68B-4R1-23-29 with (e) the presence of rare plagioclase feldspar (f) and secondary (replacive) olivine mantling partially dissolved orthopyroxene porphyroclast. (e) Talc-amphibole altered (t-aa) harzburgite 68B-1R1-10-13, showing replacement of orthopyroxene by talc (Tlc) and tremolite (Tr), and (f) talc-schist 68B-1R1-1-6. Image (a) is under plane polarized light; images in (b-h) are under cross-nicols.

Figure 3. Plot of MgO/SiO_2 vs. Al_2O_3/SiO_2 for all studied serpentinites (top panel, Type I serpentinites, bottom panel, Type II melt-impregnated and Type III metasomatic serpentinites). The lighter shaded samples (light yellow, light blue and pink) of the same shape here and in all other figures are Expedition 357 Atlantis Massif peridotites from Früh-Green et al. (2016); light orange circles and squares harzburgites and dunites, respectively, from IODP Site U1309 Atlantis Massif peridotites (Godard et al., 2009). Global abyssal peridotite data from Niu (2004), Paulick et al. (2006) and Godard et al. (2008), unless stated otherwise. Fields of serpentinized peridotite and talc-altered

peridotite are from Paulick et al. (2006) and melt-impregnated peridotites (MIP) are from Paulick et al. (2006), Godard et al. (2008) and as referenced in Whattam et al. (2011). DMM (depleted MORB mantle) and PM (primitive mantle) from Workman and Hart (2005) and Palme and O'Neill (1983) respectively. The terrestrial array is from Jagoutz (1979).

Figure 4. Variation diagrams of MgO vs. (a) SiO_2, (b) Fe_2O_3, (c) Al_2O_3, (d) CaO and (e) LOI of Atlantic Massif serpentinites from this study, and peridotites of Godard et al. (2009) and Früh-Green et al. (2018) compared with global MOR peridotite and bulk compositions of serpentine and talc (Blanco-Quintero et al. 2011, mean of ten and eight serpentine and talc analyzes). Symbols as in Fig. 3.

Figure 5. (a-e) Chondrite-normalized REE and (f-j) primitive mantle-normalized incompatible element plots of Atlantis Massif serpentinites from this study and peridotites of the study of Früh-Green et al. (2018). Chondrite and primitive mantle values are from McDonough and Sun (1995). Shown for comparison is mean abyssal peridotite composition determined on the compilations of Niu (2004) and Bodinier and Godard (2003) by Godard et al. (2008), and depleted MORB mantle (DMM) (Workman and Hart, 2005).

Figure 6. IODP Expedition 357 serpentinite samples from this study, and peridotites of the study of Früh-Green et al. (2018) on plots of (a) U and (b) Sr vs. site. Note that three of the four high-CaO Type I serpentinites (with 5.59-10.50 wt.% CaO) also exhibit the highest concentrations of Sr (> 1000 µg/g). Symbols as in Fig. 3.

800 Figure 7. Expedition 357 Atlantis Massif serpentinites from this study and peridotites of
801 the study of Früh-Green et al. (2018) in plots of (a) Th, (b) Hf, (c) Zr, (d) Ce/Yb and (e)
802 total REE vs. site. Plotted for comparison are the ranges of fluid-rock dominated and melt-
803 rock dominated global abyssal peridotite (GAP, references as in the caption for Fig. 5).
804 Depleted mantle (DM) and primitive mantle (PM) compositions are from Workman and
805 Hart (2005) and Lyubetskaya and Korenaga (2007), respectively. Symbols as in Fig. 3.
806
807 Figure 8. Primitive mantle-normalized plots of the mean compositions of (a) global
808 abyssal peridotites interpreted as being dominated by fluid-rock and melt-rock reactions,
809 (b) Atlantis Massif serpentinites from this study and (c) central serpentinites parsed into
810 site. The fluid-rock dominated peridotite is from Paulick et al. (2006) and represent
811 peridotites collected during ODP Leg 209, Sites 1268, 1772, 1274. The melt-rock
812 dominated peridotite is from Niu (2004) and Paulick et al. (2006) and in the case of
813 Paulick et al. (2006), represent peridotites collected from ODP Leg 209, Sites, 1270,
814 1271. Symbols as in Fig. 3
815
816 Figure 9. Expedition 357 Atlantis Massif serpentinites from this study and peridotites of
817 the studies of Godard et al. (2009) and Früh-Green et al. (2018) in plots of (a, b) Nb vs.
818 La, and (c, d) Ti vs. Dy. Element abundances listed as '0' were assumed to be below
819 detection limit and not used in calculation of the regression. Colors of the regressed lines
820 and text for the Expedition 357 serpentinites include: blue, western; red, central; and
821 black, eastern. In (b) and (d), the light blue, pink and light grey regressed lines represent
822 mean of the western, central and eastern sites (i.e., the blue, red and black lines in (a) and
823 (c)). R^2 values shown for Exp. 357 serpentinites represent ones which include the
824 peridotite samples of Früh-Green et al. (2018) in addition to the serpentinites from this

study and the numbers in italics in brackets beside R^2 values represent number of samples used in regression calculation. The orange line represents the dataset of Atlantis Massif peridotites from Site U1309 (Godard et al., 2009). Linearly regressed vectors (grey) labelled *A*, *B*, and *C* in (a) and (c) represent data from global abyssal peridotite (GAP) and for visual clarity, samples are omitted from the plot. The *A* trend represents the dataset of Niu (2004) which was interpreted by Paulick et al. (2006) as being representative of dominant melt-rock interaction (i.e., melt-impregnation); *B* and *C* are from Paulick et al. (2006) and represent peridotites interpreted as having compositions dominantly associated with melt-rock reaction (*B*, ODP Leg 209, MAR, Sites, 1270, 1271) and fluid-rock reaction (*C*, Sites 1268, 1772, 1274). Depleted mantle (DM) and primitive mantle (PM) compositions from Workman and Hart (2005) and Lyubetskaya and Korenaga (2007), respectively. Symbols as in Fig. 3.

Figure 10. (a) REE compositions of the most melt-depleted sample from each site compared with model estimates of 10, 15, and 20 % partial melting of DMM as well as three 'best fit' models of melting and subsequent refertilization to estimate the extent of melting experienced by these samples. Modeling is of non-modal fractional melting (dashed curves encompassing light green shade) of partial melting in % (10, 15, 20) of a four phase DMM spinel lherzolite source comprising ol: opx: cpx: sp in modal proportions of 0.53: 0.27: 0.17: 0.03 and a melt mode of -0.06: 0.28: 0.67: 0.11 (Hellebrand et al. 2002). Initial source composition, DMM from Workman and Hart (2005). Partition coefficients from Suhr et al.,1998; missing REE interpolated. Also indicated are compositions of rocks after 20 % non-modal fractional melting and subsequent 1 % or 10 % addition of a mafic melt (mm, uppermost grey shaded area) with a REE composition of the most enriched sample (eastern site M0068A-1R1-34-35 talc-

schist, Früh-Green et al., 2018, see Fig. 4e) as a proxy for a slightly LREE-enriched melt (darker green shade). Symbols as in Fig. 3.

Table captions

Table 1 Evidence and means for classification of Expedition 357 serpentinites subjected to melt-impregnation and (silica) metasomatism.

Table 2 Mineralogy and modalogy of Expedition 357 serpentinites.

Table 3 Whole rock ICP-AES and ICP-MS analyses of Expedition 357 Atlantis Massif serpentinites from this study.

Supplementary material

See Supplementary Document

References

Absalov, M.Z., 1998. Chrome-spinels in gabbro-wehrlite intrusions of the Pechenga area, Kola Peninsula, Russia: emphasis on alteration features. Lithos 43, 109-134.

Andreani, M., Mével, C., Boullier, A.-M., Escartin, J., 2007. Dynamic control on serpentine crystallization in veins: constraints on hydration processes in oceanic peridotites. Geochemistry, Geophysics, Geosystems 8 (2), Q02012.

Akizawa, N., Früh-Green, G.L., Tamura, A., Tamura, C., Morishita, T., 2020. Compositional heterogeneity and melt transport in mantle beneath Mid-Atlantic Ridge constrained by peridotite, dunite, and wehrlite from Atlantis Massif. Lithos 354-355, 105364. https://doi.org/10.1016/j.lithos.2019.105364.

Andreani, M., Mevel, C., Boullier, A.-M., Escartin, J., 2007. Dynamic control on serpentine crystallization in veins: constraints on hydration processes in oceanic peridotites. Geochemistry, Geophysics, Geosystems 8.

877 Arai, S., Abe, N., Hirai, H., 1998. Petrological characteristics of the sub-arc mantle: An overview on
878 petrology of peridotite xenoliths from the Japan Arcs. Trends in Mineralogy 2, 39-55.
879 Arai, S., Matsukage, K., 1996. Petrology of gabbro-troctolite–peridotite complex from Hess Deep,
880 equatorial Pacific: implications for mantle–melt interaction within the oceanic lithosphere. In: Mével,
881 C., Gillis, K.M., Allan, J.F., Meyer, P.S. (Eds.), Proceedings of the Ocean Drilling Program: Scientific
882 Results, 147, pp. 135-155.
883 Arai, S., Shimizu, Y., Ismail, S.A., Ahmed, A.H., 2006. Low-T formation of high-Cr spinel with apparently
884 primary chemical characteristics within podiform chromitite from Rayat, northeastern Iraq.
885 Mineralogical magazine 70(5), 499-508.
886 Aswad, K.J.A., Aziz, N.R.H., Koyi, H.A., 2011. Cr-spinel compositions in serpentinites and their
887 implications for the petrotectonic history of the Zagros Suture Zone, Kurdistan Region, Iraq. Geological
888 Magazine 148(5-6), 802-818. doi:10.1017/S0016756811000422.
889 Bach, W., Klein, F. 2009. The petrology of seafloor rodingites:: Insights from geochemical reaction path
890 modelin. Lithos 112(1-2), 103-117. http://dx.doi.org/10.1016/j.lithos.2008.10.022.
891 Ballhaus, C., Berry, R.F., Green, D.H., 1991. High pressure experimental calibration of the olivine-
892 orthopyroxene-spinel oxygen barometer, implications for the oxidation of the mantle. Contributions to
893 Mineralogy and Petrology 107, 27-40.
894 Barnes, S.J., 2000. Chromite in komatiites II. Modification during greenschist to mid-amphibolite facies
895 metamorphism. Journal of Petrology, 41, 387-409.
896 Barnes, S.J., Roeder, P.L., 2001. The range of spinel compositions in terrestrial mafic and ultramafic rocks.
897 Journal of Petrology 42(12), 2279-2302.
898 Barra, F., Gervilla, F., Hernández, E., Reich, M., Padrón-Navarta, J.A., González-Jiménez, J.M., 2014.
899 Alteration patterns of chromian spinels from La Cabaña peridotite, south-central Chile. Mineralogy and
900 Petrology 108, 819-836. DOI 10.1007/s00710-014-0335-5.
901 Bedini, R.M., Bodinier, J.-L., 1999. Distribution of incompatible trace elements between the constituents
902 of spinel peridotite xenoliths: ICP-MS data from the East African Rift. Geochimica et Cosmochimica
903 Acta, 63(22), 3883-3900.
904 Bhat, I.M., Ahmad, T., Subba Rao, D.V., 2019. Alteration of primary Cr-spinel mineral composition from
905 the Suru Valley ophiolitic peridotites, Ladakh Himalaya: Their low-temperature metamorphic
906 implications. Journal of Earth System Science 128:188. https://doi.org/10.1007/s12040-019-1222-6.

907 Blackman, D.K., Cann, J.R., Janssen, B., Smith, D.K., 1998. Origin of extensional core complexes:
908 evidence from the Mid-Atlantic Ridge at Atlantis Fracture Zone. Journal of Geophysical Research: Solid
909 Earth 103, 21315-21333.
910 Blackman, D.K., Karson, J.A., Kelley, D.S., Cann, J.R., Früh- Green, G.L., Gee, J.S., Hurst, S.D., John,
911 B.E., Morgan, J., Nooner, S.L., Ross, D.K., Schroeder, T.J., Williams, E.A., 2002. Geology of the
912 Atlantis Massif (Mid-Atlantic Ridge, 30º N): implications for the evolution of an ultramafic oceanic
913 core complex. Marine Geophysical Researches 23, 443-469.
914 Blackman, D.K., Ildefonse, B., John, B.E., Ohara, Y., Miller, D.J., MacLeod, C.J., 2006. Proceedings of
915 the IODP, 304/305. College Station TX. doi:10.2204/iodp.proc.304305.2006. (Integrated Ocean Drilling
916 Program Management International, Inc.).
917 Blanco-Quintero, I.F., Proenza, J.A., García-Casco, A., Tauler, E., Galí, S., 2011. Serpentinites and
918 serpentinites within a fossil subduction channel: La Corea mélange, eastern Cuba. Geologica Acta 9 (3-
919 4), 389-405. DOI :10.1344/105.000001662.
920 Bodinier, J.L., Godard, M., 2003. Orogenic, ophiolitic, and abyssal peridotites. Treatise on Geochemistry,
921 vol. 2. Elsevier, Amsterdam, pp. 103-170.
922 Bodinier, J.L., Menzies, M.A., Thirlwall, M.F., 1991. Continental to oceanic mantle transition: REE and
923 Sr–Nd isotopic geochemistry of the Lanzo Lherzolite Massif. Journal of Petrology Special Volume 2,
924 191-210.
925 Boschi, C., Früh-Green, G.L., Delacour, A., Karson, J.A., Kelley, D.S., 2006a. Mass transfer and fluid flow
926 during detachment faulting and development of an oceanic core complex, Atlantis Massif (MAR 30°N).
927 Geochemistry, Geophysics Geosystems 7 (1), Q01004.
928 Boschi, C., Früh-Green, G.L., Escartin, J., 2006b. Occurrence and significance of serpentinite-hosted, talc-
929 rich fault rocks in modern oceanic settings and ophiolite complexes. Ofioliti 31 (2), 123–134.
930 Boschi, C., Dini, A., Früh-Green, G.L., Kelley, D.S., 2008. Isotopic and element exchange during
931 serpentinization and metasomatism at the Atlantis Massif (MAR 30°N): insights from B and Sr isotopes.
932 Geochimica et Cosmochimica Acta 72 (7), 1801–1823.
933 Burkhard, D.J.M., 1993. Accessory chromian spinels: Their coexistence and alteration in serpentinites.
934 Geochimica et Cosmochimica Acta 57, 1297-1306.
935 Cannat, M., 1993. Emplacement ofmantle rocks in the seafloor at mid-ocean ridges. Journal of Geophysical
936 Research: Solid Earth 98 (B3), 4163-4172.

Cannat, M., Karson, J.A., Miller, D.J., Agar, S.M., Barling, J., Casey, J.F., Ceuleneer, G., Dilek, Y., Fletcher, J.M., Fujibayashi, N., Gaggero, L., Gee, J.S., Hurst, S.D., Kelley, D.S., Kempton, P.D., Lawrence, R.M., Marchig, V., Mutter, C., Niida, K., Rodway, K., Ross, D.K., Stephens, C.J., Werner, C.-D. and Whitechurch, H., 1995. Mid-Atlantic Ridge: Sites 920–924. Proc. ODP, Initial Reports, 153. Ocean Drilling Program, Texas A&M University, College Station, TX, United States.

Cann, J.R., Blackman, D.K., Smith, D.K., McAllister, E., Janssen, B., Mello, S., Avgerinos, E., Pascoe, A.R., Escartín, J., 1997. Corrugated slip surfaces formed at ridge-transform intersections on the Mid-Atlantic Ridge. Nature 385, 329-332.

Dare, S.A.S., Pearce, J.A., McDonald, I., Styles, M.T., 2009. Tectonic discrimination of peridotites using fO_2–Cr# and Ga–Ti–Fe^{III} systematics. Chemical Geology 261, 199-216.

Deschamps, F., Guillot, S., Godard, M., Chauvel, C., Andreani, M., Hattori, K., 2010. In situ characterization of serpentinites from forearc mantle wedges: Timing of serpentinization and behavior of fluid-mobile elements in subduction zones. Chemical Geology 269, 262-277. http://dx.doi.org/10.1016/j.chemgeo.2009.10.002.

Dick, H.J.B., Bullen, T., 1984. Chromian spinel as a petrogenetic indicator in abyssal and alpine-type peridotites and spatially associated lavas. Contributions to mineralogy and petrology 86, 54-76.

Dick, H.J.B., Natland, J.H., Alt, J.C., Bach,W., Bideau, D., Gee, J.S., Haggas, S., Hertogen, J.G.H., Hirth, G., Holm, P.M., Ildefonse, B., Iturrino, G., John, B.E., Kelley, D.S., Kikawa, E., Kingdon, A., LeRoux, P.J., Maeda, J., Meyer, P.S., Miller, D.J., Naslund, H.R., Niu, Y., Robinson, P.T., Snow, J.E., Stephen, R.A., Trimby, P.W.,Worm, H.-U., Yoshinobu, A., 2000. A long in situ section of the lower ocean crust: results of ODP Leg 176 drilling at the Southwest Indian Ridge. Earth and Planetary Science Letters 179, 31-51.

Dick, H.J.B., Tivey, M.A., Tucholke, B.E., 2008. Plutonic foundation of a slow-spreading ridge segment: Oceanic core complex at Kane Megamullion, 23° 30'N, 45 °20'W. Geochemistry, Geophysics, Geosystems 9, Q05014. doi:10.1029/2007GC001645.

Donnelly, K.E., Goldstein, S.L., Langmuir, C.H., Spiegelman, M., 2004. Origin of enriched ocean ridge basalts and implications for mantle dynamics. Earth and Planetary Science Letters, 226, 347-366.

964 Drouin, M., Godard, M., Ildefonse, B., Bruguier, O., Garrido, C.J., 2009. Geochemical and petrographic
965 evidence for magmatic impregnation in the oceanic lithosphere at Atlantis Massif,Mid-Atlantic Ridge
966 (IODP Hole U1309D, 30°N). Chemical Geology 264, 71-88.
967 Elderfield, H. and Greaves, M.J., 1982. The rare earth elements in seawater. Nature 296, 214-219.

968 Escartín, J., Mével, C., MacLeod, C.J., and McCaig, A.M., 2003, Constraints on deformation conditions
969 and the origin of oceanic detachments: The Mid-Atlantic Ridge core complex at 15°45'N: Geochemistry,
970 Geophysics, Geosystems, v. 4, no. 8, p. 1067, doi:10.1029/2001GC000278.

971 Escartin, J., Mével, C., Petersen, S., Bonnemains, D., Cannat, M., Andeani, M., Augustin, N., Bezos, A.,
972 Chavagnac, V., Choi, Y., Godard, M., Haaga, K., Hamelin, C., Ildefonsa, B., Jamieson, J., John, B.,
973 Leleu, T., MacLeod, C.J., Massot-Campos, M., Nomikou, P., Olive, J.A., Paquet, M., Rommevaux, C.,
974 Rothenbeck, M., Steinfuhrer, Tominaga, M., Triebe, L., Campos, R., Gracias, N., Garcia, R., 2017.
975 Tectonic structure, evolution, and the nature of oceanic complexes and their detachment zones (13º20′N
976 and 13º30′N, Mid Atlantic Ridge). Geochemistry, geophysics, geosystems. doi:
977 10.1002/2016GC006775.
978 Evans, B.W., Frost, B.R., 1975. Chrome-spinel in progressive metamorphism; a preliminary analysis.
979 Geochimica et Cosmochimica Acta, 39, 959-972.
980 Evans, B.W., Trommsdorff, V., 1970. Regional metamorphism of ultramafic rocks in the Central Alps
981 Paragenesis in the system CaO-MgO-SiO_2-H_2O. Schweiz.Min.Pen.Milt. 50, 481-492.
982 Ferrando, C., Godard, M., Ildefonse, B., Rampone, E., 2018. Melt transport and mantle assimilation at
983 AtlantisMassif (IODP Site U1309): constraints from geochemical modeling. Lithos 323, 24-43.
984 Franz, L., Wirth, R., 2000. Spinel inclusions in olivine of peridotite xenoliths from TUBAF seamount
985 (Bismark Archipelago/Papua New Guinea): evidence for the thermal and tectonic evolution of the
986 oceanic lithosphere. Contributions to Mineralogy and Petrology 140, 283-295.
987 Frisby, C., Bizimis, M., Mallick, S., 2016a. Hf-Nd isotope decoupling in bulk abyssal peridotites due to
988 serpentinization. Chemical Geology 440, 60-72. http://dx.doi.org/10.1016/j.chemgeo.2016.07.006.
989
990 Frisby, C., Bizimis, M., Mallick, S., 2016b. Seawater-derived rare earth element addition to abyssal
991 peridotites during serpentinization. Lithos 248-251, 432-454.

992 Frost, B.R., Beard, J.S., McCaig, A., Condliffe, E., 2008. The formation of micro-rodingites from IODP
993 Hole U1309D: Key in understanding the process of serpentinization. Journal of Petrology 49(9), 1579-
994 1588. http://dx.doi.org/10.1093/petrology/egn038.
995 Früh-Green, G.L., Connolly, J.A.D., Plas, A., Kelley, D.S., Grobéty, B., 2004. Serpentinization of oceanic
996 peridotites: implications for geochemical cycles and biological activity. In: Wilcock, W.S.D., DeLong,
997 E.F., Kelley, D.S., Baross, J.A., Cary, C. (Eds.), The Subseafloor Biosphere at Mid-Ocean Ridges.
998 Geophysical Monograph. 144, pp. 119-136.
999 Früh-Green, G.L., Orcutt, B.N., Green, S.L., et al., 2017. Expedition 357 summary. In: Früh- Green, G.L.,
1000 Orcutt, B.N., Green, S.L., Cotterill, C. (Eds.), Expedition 357 Scientists. Proceedings of the International
1001 Ocean Discovery Program 357, College Station, TX. https://doi.org/10.14379/iodp.proc.357.101.2017.
1002 Früh-Green, G.L., Orcutt, B.N., Green, S., Cotterill, C., and the Expedition 357 Scientists, 2016. Expedition
1003 357 Preliminary Report: Atlantis Massif Serpentinization and Life. International Ocean Discovery
1004 Program. 10.14379/iodp.pr.357.2016
1005 Früh-Green, G.L., Orcutt, B.N., Rouméjon, S., et al., 2018. Magmatism, serpentinization and life: insights
1006 through drilling the Atlantis Massif (IODP Expedition 357). Lithos 323, 137-155.
1007 https://doi.org/10.1016/j.lithos.2018.09.012.
1008 Gargiulo, M.F., Bjerg, E.A., Mogessie, A., 2013. Spinel group minerals in metamorphosed ultramafic rocks
1009 from Río de Las Tunas belt, Central Andes, Argentina. Geologica Acta 11(2), 133-148. doi : 10.1344 /
1010 105 .000001836.
1011 Grimes, C.B., John, B.E., Cheadle, M.J., Wooden, J.L., 2008. Protracted construction of gabbroic crust at
1012 a slow spreading ridge: constraints from 206Pb/238U zircon ages from Atlantis Massif and IODP Hole
1013 U1309D (30°N, MAR). Geochemistry, Geophysics, Geosystems 9 Q08012.
1014 Godard, M., Lagabrielle, Y., Alard, O., Harvey, J., 2008. Geochemistry of the highly depleted peridotites
1015 drilled at ODP Sites 1272 and 1274 (Fifteen–Twenty Fracture Zone, Mid-Atlantic Ridge): implications
1016 for mantle dynamics beneath a slow spreading ridge. Earth and Planetary Science Letters 267 (3-4), 410–
1017 425. doi:10.1016/j.epsl.2007.11.058.
1018 Godard, M., Awaji, S., Hansen, H., et al., 2009. Geochemistry of a long in-situ section of intrusive slow-
1019 spread oceanic lithosphere: results fromIODP Site U1309 (Atlantis Massif, 30°N Mid-Atlantic-Ridge).
1020 Earth and Planetary Science Letters 279, 110-122.

González-Jiminéz, J.M., Kerestedjian, T., Proenza, J.A., Gervilla, F., 2009. Metamorphism on Chromite Ores from the Dobromirtsi Ultramafic Massif, Rhodope Mountains (SE Bulgaria). Geologica Acta 67, 7(4), 413-429. DOI: 10.1344/104.000001447.

Hart, S.R., Zindler, A., 1986. In search of a bulk-earth composition. Chemical Geology 57, 247-267.

Heinrich, K.F.J., 1987. Mass absorption coefficients for electron probe microanalysis. In: Brown, J. Packwood, R. (Eds.), Proceedings of the 11th International Congress on X-Ray Optics and Microanalysis, University of Western Ontario, London, Ontario, Canada 1986, pp. 67-119.

Hellebrand, E., Snow, J.E., Dick, H.J.B., Hofmann, A.W., 2001. Coupled major and trace elements as indicators of the extent of melting in mid-ocean-ridge peridotites. Nature 410, 677-681.

Ildefonse, B., Blackman, D.K., John, B.E., Ohara, Y., Miller, D.J., MacLeod, C.J., 2007. Oceanic core complexes and crustal accretion at slow-speading ridges. Geology 35, 623-626.

Irvine, T.N., 1967. Chromian spinel as a petrogenetic indicator Part 2, petrologic applications. Canadian Journal of Earth Sciences 4, 71-103.

Jagoutz, E., Palme, H., Baddenhausen, H., Blum, K., Cendales, M., Dreibus, G., Spettel, B., Lorenz, V., Vanke, H., 1979. The abundance of major, minor and trace elements in the earth's mantle as derived from primitive ultramafic nodules. Geochimica et Cosmochimica Acta 11 (2), 2031-2050.

Karson, J.A., 2002. Geologic structure of the uppermost oceanic crust created at fast- to intermediate-rate spreading centers. Annual Review of Earth and Planetary Sciences 30, 347–384.

Karson, J.A., Früh-Green, G.L., Kelley, D.S., Williams, E.A., Yoerger, D.R., Jakuba, M., 2006. Detachment shear zone of the Atlantis Massif core complex, Mid-Atlantic Ridge, 30°N. Geochemistry, Geophysics Geosystems 7 (6), Q06016.

Kelemen, P.B., 1990. Reaction between ultramafic rock and fractionating basaltic magma I. Phase relations, the origin of calc-alkaline magma series, and the formation of discordant dunite. Journal of Petrology 31, 51-98.

Kelemen, P.B., Hirth, G., Shimizu, N., Spiegelman, M., Dick, H., 1997. A review of melt migration processes in the adiabatically upwelling mantle beneath oceanic spreading ridges. Philosophical Transactions of the Royal Society of London. Series A355, 283-318.

Kelemen, P., Kikawa, E., Miller, J., Abe, N., Bach,W., Carlson, R.L., Casey, J.F., Chambers, L.M., Cheadle, M., Cipriani, A., Dick, H.J.B., Faul, U., Garces, M., Garrido, C., Gee, J.S., Godard, M., Griffin, D.W., Harvey, J., Ildefonse, B., Iturrino, G.J., Josef, J., Meurer,W.P., Paulick, H., Rosner, M., Schroeder,

T., Seyler, M., Takazawa, E. and Mrozewski, S., 2004. Drilling Mantle Peridotite along the Mid-Atlantic Ridge from 14° to 16°N: Sites 1268-1275. Proc. ODP, Initial Reports, 209. Ocean Drilling Program, Texas A&M University, College Station TX 77845-9547, USA. doi:10.2973/odp.proc.ir.209.2004 pp.

Kelemen, P.B., Kikawa, E., Miller, D.J., Shipboard Scientific Party, 2007. Leg 209 summary: processes in a 20-km-thick conductive boundary layer beneath the Mid-Atlantic Ridge, 14°–16°N. In: Kelemen, P.B., Kikawa, E., Miller, D.J. (Eds.), Proceedings of the Ocean Drilling Program, Scientific Results, 209: College Station, TX. Ocean Drilling Program, pp. 1-33.

Kelemen, P.B., Shimizu, N., Salters, V.J.M., 1995. Extraction of mid-ocean-ridge basalt from the upwelling mantle by focused flow of melt in dunite channels. Nature 375, 747-753.

Kelley, D.S., Karson, J.A., Blackman, D.K., Fruh-Green, G.L., Butterfield, D.A., Lilley, M.D., Olson, E.J., Shrenk, M.O., Roe, K.K., Lebon, G.T., Rivizzigno, P., 2001. An off-axis hydrothermal vent field discovered near the Mid-Atlantic Ridge at 30°N. Nature 412, 145-149.

Khalil, K.I., El-Makky, A.M., 2009. Alteration Mechanisms of Chromian-Spinel during Serpentinization at Wadi Sifein Area, Eastern Desert, Egypt. Resource Geology 59(2), 194-211. doi: 10.1111/j.1751-3928.2009.00090.x.

Kimball, K.L. (1990) Effects of hydrothermal alteration on the compositions of chromian spinels. Contributions to Mineralogy and Petrology, 105, 337-346.

Leybourne, M.I., Peter, J.M., Layton-Mathews, D., Volesky, J., Boyle, D.R., 2006. Mobility and fractionation of rare earth elements during supergene weathering and gossan formation and chemical modification of massive sulphide gossan. Geochimica et Cosmochimica Acta 70(5), 1097-1112. https://doi.org/10.1016/j.gca.2005.11.003

Lenoir, X., Garrido, C.J., Bodinier, J.-L., Dautria, J.-M., Gervilla, F., 2001. The recrystallization front of the Ronda peridotite: evidence for melting and thermal erosion of subcontinental lithospheric mantle beneath the Alboran Basin. Journal of Petrology 42, 141-158.

Liebmann, J., Schwarzenbach, E.M., Früh- Green, G.L., Boschi, C., Rouméjon, S., Strauss, H., Wiechert, U., John, T., 2018. Tracking Water- Rock Interaction at the Atlantis Massif (MAR, 30°N) using sulfur geochemistry. Geochemistry, geophysics, geosystems, 19(11), 4561-4583. doi:10.1029/2018GC007813.

Lyubetskaya, T., Korenaga, J., 2007. Chemical composition of Earth's primitive mantle and its variance: 1. Method and resultsJournal of Geophysical Research 12, B03211. doi:10.1029/2005JB004223.

1080 Macdonald, K.C., 1982. Mid-ocean ridges: fine scale tectonic, volcanic and hydrothermal processes within
1081 the plate boundary zone. Annual Review of Earth and Planetary Sciences 10, 155-190.
1082 McCaig, A.M., Cliff, R.A., Escartin, J., Fallick, A.E., MacLeod, C.J., 2007. Oceanic detachment faults
1083 focus very large volumes of black smoker fluids. Geology 35 (10), 935-938.
1084 McCaig, A.M., Delacour, A., Fallick, A.E., Castelain, T., Früh-Green, G.L., 2010. Fluid circulation and
1085 isotopic alteration in and beneath oceanic detachment faults in the Central Atlantic: Implications for the
1086 geometry and evolution of high-temperature hydrothermal circulation cells at slow-spreading ridges, In:
1087 Diversity of Hydrothermal Systems on Slow Spreading Ocean Ridges. In: Rona, P.A., Devey, C.W.,
1088 Dyment, J.,Murton, B.J. (Eds.), AGU Geophy. Mono. Series. 188, pp. 207–239.
1089 McDonough, W.F. and Rudnick, R.L., 1998. Mineralogy and composition of the upper mantle. In: Hemley,
1090 R.J. (Ed.), Ultrahigh pressure mineralogy: Reviews in Mineralogy, V. 37, Mineralogical Society of
1091 America, DeGruyter, pp. 139-164. https://doi.org/10.1515/9781501509179.
1092 McDonough, W.F., Sun, S.S., 1995. The composition of the Earth. Chemical Geology 120, 223-253.
1093 Merlini, A., Grieco, G., Diella, V., 2009. Ferritchromite and chromian-chlorite formation in mélange-hosted
1094 Kalkan chromitite (Southern Urals, Russia). American Mineralogist 94, 1459-1467.
1095 Müntener, O., Pettke, T., Desmurs, L., Meier, M., Schaltegger, U., 2004. Refertilization of mantle peridotite
1096 in embryonic ocean basins: trace element and Nd isotopic evidence and implications for crust–mantle
1097 relationships. Earth and Planetary Science Letters 221, 293-308. doi:10.1016/S0012-821X(04)00073-1.
1098 Niida, K., 1997. Mineralogy of MARK peridotites: replacement through magma channeling examined from
1099 920D, MARK area. In: Karson, J.A., Cannat, M., Miller, D.J., Elthon, D. (Eds.), Proceedings of the
1100 Ocean Drilling Program: Scientific Results,153. Ocean Drilling Program, College Station, TX, pp. 265-
1101 275.
1102 Niu, Y., 1997. Mantle melting and melt extraction processes beneath ocean ridges: evidence from abyssal
1103 peridotites. Journal of Petrology 38, 1047-1074.
1104 Niu, Y., 2004. Bulk rock major and trace element compositions of abyssal peridotites: implications for
1105 mantle melting, melt extraction and post-melting processes beneath mid-ocean ridges. Journal of
1106 Petrology 45, 2423-2458.
1107 Obata M., Banno, S., Mori, T., 1974. The iron-magnesium partitioning between naturally occurring
1108 coexisting olivine and Ca-rich clinopyroxene: an application of the simple mixture model to olivine solid
1109 solution. Bull. Soc. Jr. Miner. Crystallogr., 97, 101-107.

1110 O'Hanley, D.S., 1996. Serpentinites Records of Tectonic and Petrological History. Oxford, Oxford
1111 University Press, 290 pp.
1112 Palme, H., O'Neill, H.S.C., 2003. Cosmochemical estimates of mantle composition, In: Treatise on
1113 Geochemistry, vol. 2, Holland, H., Turekian, K.K., (Eds.), pp. 1-38, Elsevier, New York.

1114 Parnell-Turner, R., Escartín, J., Olive, J.-A., Smith, D.K., and Petersen, S., 2018, Genesis of corrugated
1115 fault surfaces by strain localization recorded at oceanic detachments: Earth and Planetary Science Letters,
1116 v. 498, p. 116–128, doi: 10.1016/j.epsl.2018.06.034.

1117 Parkinson, I.J., Pearce, J.A., 1998. Peridotites from the Izu–Bonin–Mariana Forearc (ODP Leg 125),
1118 evidence for mantle melting and melt–mantle interaction in a suprasubduction zone setting. Journal of
1119 Petrology 39, 1577-1618.
1120 Paulick, H., Bach,W., Godard, M., De Hoog, J.C.M., Suhr, G., Harvey, J., 2006. Geochemistry of abyssal
1121 peridotites (Mid-Atlantic Ridge, 15°20′N, ODP Leg 209): implications for fluid/rock interaction in slow
1122 spreading environments. Chemical Geology 234, 179-210.
1123 Picazo, S., Cannat, M., Delacour, A., Escartin, J., Rouméjon, S., Silantyev, 2012. Deformation associated
1124 with the denudation of mantle-derived rocks at the Mid-Atlantic Ridge 13°-15°N: The role of magmatic
1125 injections and hydrothermal alteration. Geochemistry, geophysics, geosystems 13(9).
1126 https://doi.org/10.1029/2012GC004121
1127 Pouchou, J.-L., Pichoir, F., 1991. Quantitative analysis of homogeneous or stratified microvolumes
1128 applying the model "PAP". In: Heinrich, K.F.J., Newbury, D.E. (Eds.), Electron Probe Quantitation
1129 Plenum Publishing Corporation, New York, New York, pp. 31-75.
1130 Purvis, A.C., Nesbitt, R.W., Hallberg, J.A., 1972. The geology of the part of the Carr Boyd rocks complex
1131 and it's associated nickel mineralization, Western Australia. Economic Geology 67, 1093-1113.
1132 Quick, J.E., 1981. The origin and significance of large, tabular dunite bodies in the Trinity peridotite,
1133 northern California. Contributions to Mineralogy and Petrology 78, 413-422.
1134 Rampone, E., Piccardo, G.B.,Vannucci, R., Bottazzi, P., 1997. Chemistry and origin of trapped melts in
1135 ophiolitic peridotites. Geochimica et Cosmochimica Acta 61, 4557-4569.
1136 Rampone, E., Piccardo, G.B., Vannucci, R., Bottazzi, P., Zanetti, A., 1994. Melt impregnation in ophiolitic
1137 peridotite: an ion microprobe study of clinopyroxene and plagioclase. Mineralogical Magazine 58A,
1138 756-757.

1139 Reed, S.J.B., 1990), Fluorescence effects in quantitative microprobe analysis. In: Williams, D.B., Ingram,
1140 P., Michael, J.R. (Eds.), Microbeam Analysis-1990 San Francisco Press, San Francisco, pp. 109-114.
1141 Rouméjon, S., Cannat, M., Agrinier, P., Godard, M., Andreani, M., 2015. Serpentinization and Fluid
1142 Pathways in Tectonically Exhumed Peridotites from the Southwest Indian Ridge (62-65 E). Journal of
1143 Petrology 56, 703-734.
1144 Rouméjon, S., Früh-Green, G.L., Orcutt, B.N., the IODP Expedition 357 Science Party, 2018a. Alteration
1145 heterogeneities in peridotites exhumed on the southern wall of the Atlantis Massif (IODP Expedition
1146 357). Journal of Petrology, 1–29 https://doi.org/10.1093/petrology/egy065.
1147 Rouméjon, S.,Williams, M.J., Früh-Green, G.L., 2018b. In situ oxygen isotope analyses in serpentine
1148 minerals: constraints on serpentinization during tectonic exhumation at slow- and ultraslow-spreading
1149 ridges. Lithos 323, 156-173. https://doi.org/10.1016/j.lithos.2018.09.021.
1150 Sack R.O., Ghiorso M.S., 1991. Chromian spinels as petrogenetic indicators: thermodynamic and
1151 petrological applications. American Mineralogist 76, 827-847.
1152 Säntii, J., Kontinen, A., Sorjonen-Ward, P., Johanson, B., Pakkanen, L., 2006. Metamorphism and
1153 Chromite in Serpentinized and Carbonate-Silica-Altered Peridotites of the Paleoproterozoic Outokumpu-
1154 Jormua Ophiolite Belt, eastern Finland. International Geology Review 48, 494-546.
1155 https://doi.org/10.2747/0020-6814.48.6.494.
1156 Saumur, B.M., Hattori, K. 2013. Zoned Cr-spinel and ferritchromite alteration in forearc mantle
1157 serpentinites of the Rio San Juan Complex, Dominican Republic. Mineralogical Magazine 77(1), 117-
1158 136. DOI: 10.1180/minmag.2013.077.1.11.
1159 Schroeder, T., John, B.E., 2004. Strain localization on an oceanic detachment fault system, Atlantis Massif,
1160 30° N, Mid-Atlantic Ridge. Geochemistry, Geophysics, Geosystems 5.
1161 Schroeder, T., John, B.E., and Frost, B.R., 2002, Geologic implications of seawater circulation through
1162 peridotite exposed at slow-spreading mid-ocean ridges, Geology, v. 40, p. 367-370.
1163 Shibata T., Thompson, G. 1986. Peridotites from the mid-Atlantic ridge at 43 °N and their petrogenetic
1164 relation to abyssal tholeiites. Contribution to Mineralogy and Petrology 93, 144-159.
1165 Snow, J.E., Dick, H.J.B., 1995. Pervasive magnesium loss by marine weathering of peridotite. Geochimica
1166 et Cosmochimica Acta 59 (20), 4219-4235.
1167 Spangenberg, K., 1943. Die Chromitlagerstatte von Tampadel am Zobten. Zeitschrift fur Praktische
1168 Geologie 51, 13-35.

1169 Springer, G., 1971. Fluorescence by the X-ray continuum in multi-element targets: Falconbridge Nickel
1170 Mines Limited, Thornhill, Ontario, Canada, Report FRL-138, 14 p.
1171 Starr, P., 2017. Sub-Greenschist to Lower Amphibolite Facies Metamorphism of Basalts: Examples from
1172 Flin Flon, Manitoba and Rossland, British Columbia. Ph.D. thesis, University of Calgary, 495 pp.
1173 Stevens, R.E., 1944. Composition of some chromites of the Western hemisphere. American Mineralogist
1174 29, 1-34.
1175 Stewart, M.A., Karson, J.A., Klein, E.M., 2005. Four-dimensional upper crustal construction at fast-
1176 spreading mid-ocean ridges: a perspective from an upper crustal cross-section at the Hess Deep Rift.
1177 Journal of Volcanology and Geothermal Research 144, 287-309.
1178 Su, Y., 2003. Global MORB chemistry compilation at the segment scale. Ph.D. Thesis. New York,
1179 Columbia University.
1180 Suita, M.T., Streider, A.J., 1996. Cr-Spinels from Brazilian mafic - ultramafic complexes: metamorphic
1181 modifications. International Geology Review 38, 245-267.
1182 Suhr, G., Hellebrand, E., Johnson, K., Brunelli, D., 2008. Stacked gabbro units and intervening mantle: a
1183 detailed look at a section of IODP Leg 305, Hole U1309D. Geochemistry, Geophysics, Geosystems 9.
1184 https://doi.org/10.1029/2008GC002012.
1185 Suhr, G., Hellebrand, E., Snow, J.E., Seck, H.A., Hofmann, A.W., 2003. Significance of large, refractory
1186 dunite bodies in the upper mantle of the Bay of Islands Ophiolite. Geochemistry, Geophysics,
1187 Geosystems 4, 8605. doi:10.1029/2001GC000277.
1188 Takazawa, E., Frey, F.A., Shimuzu, N., Obata, M., Bodinier, J.L., 1992. Geochemical evidence for melt
1189 migration and reaction in the upper mantle. Nature 359, 55-58.
1190 Tucholke, B.E., Lin, J., Kleinrock, M.C., 1998. Megamullions and mullion structure defining oceanic
1191 metamorphic core complexes on the Mid-Atlantic Ridge. Journal of Geophysical Research 103, 9857-
1192 9866.
1193 Van der Wal, D., Bodinier, J.-L., 1996. Origin of the recrystallisation front in the Ronda peridotite by km-
1194 scale pervasive porous melt flow. Contributions to Mineralogy and Petrology 122, 387-405.

1195 Verlaguet, A., Bonnemains, D., Mével, C., Escartín, J., Andreani, M., Bourdelle, F., Boiron, M. - C.,
1196 Chavagnac, V., 2021. Fluid circulation along an oceanic detachment fault: Insights from fluid inclusions
1197 in silicified brecciated fault rocks (Mid- Atlantic Ridge at 13°20′N). Geochemistry, geophysics,
1198 geosystems 22(1), 1–32. doi: 10.1029/2020GC009235.

1199 Whattam, S.A., Cho, M., Smith, I.E.M., 2011. Magmatic peridotites and pyroxenites, Andong Ultramafic
1200 Complex, Korea: Geochemical evidence for supra-subduction zone formation and extensive melt–rock
1201 interaction. Lithos 127, 599-618.
1202 Workman, R.K., Hart, S.R., 2005. Major and trace element composition of the depleted MORB mantle
1203 (DMM), Earth and Planetary Science Letters 231, 53–-72.
1204 Zervas, C.E., Sempéré, J.-C., Lin, J., 1995. Morphology and crustal structure of a small transform fault
1205 along theMid-Atlantic Ridge: the Atlantis Fracture Zone. Marine Geophysical Researches 17, 275-300.
1206 https://doi.org/10.1007/BF01203466.

Figure 1

Click here to access/download;Figure;Fig. 1 PR2.pdf

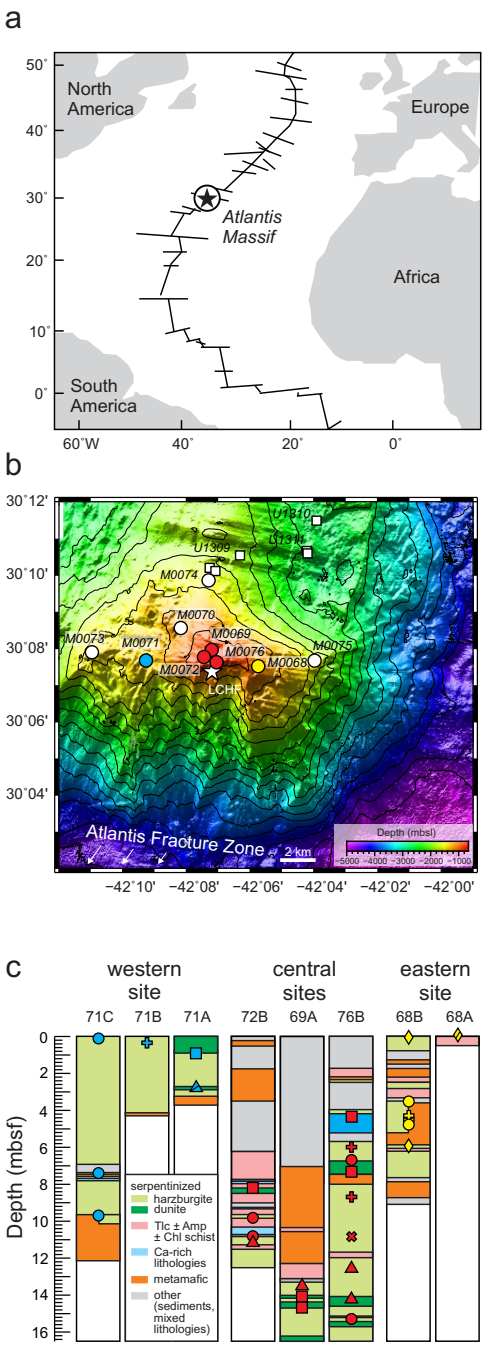

Figure 1 PR1 Whattam et al. (2021)

Figure 2

Click here to access/download;Figure;Fig. 2 PR2.pdf

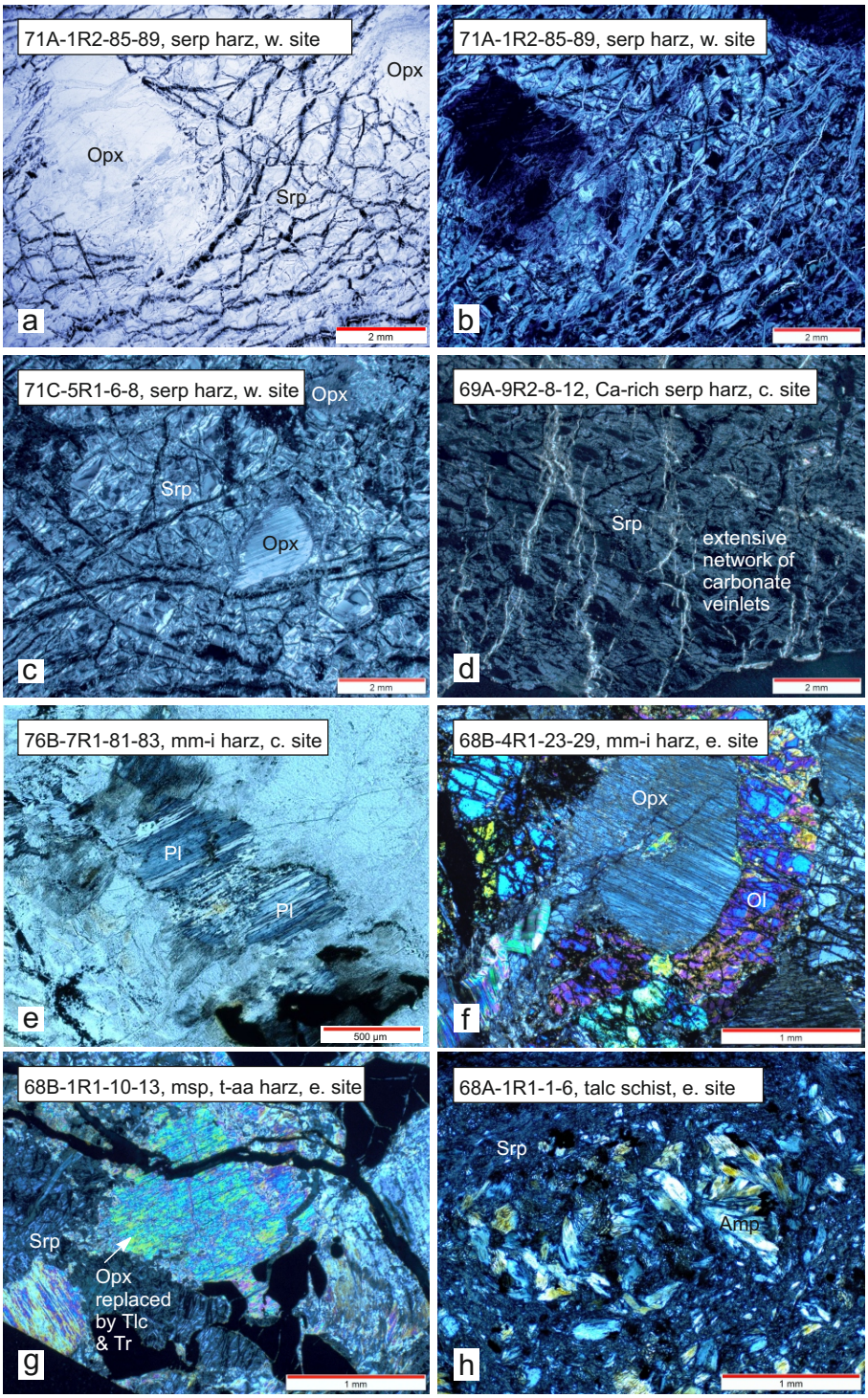

Figure 2 P-S 1A Whattam et al. (2021)

Figure 3

Click here to access/download;Figure;Fig. 3 PR2.pdf

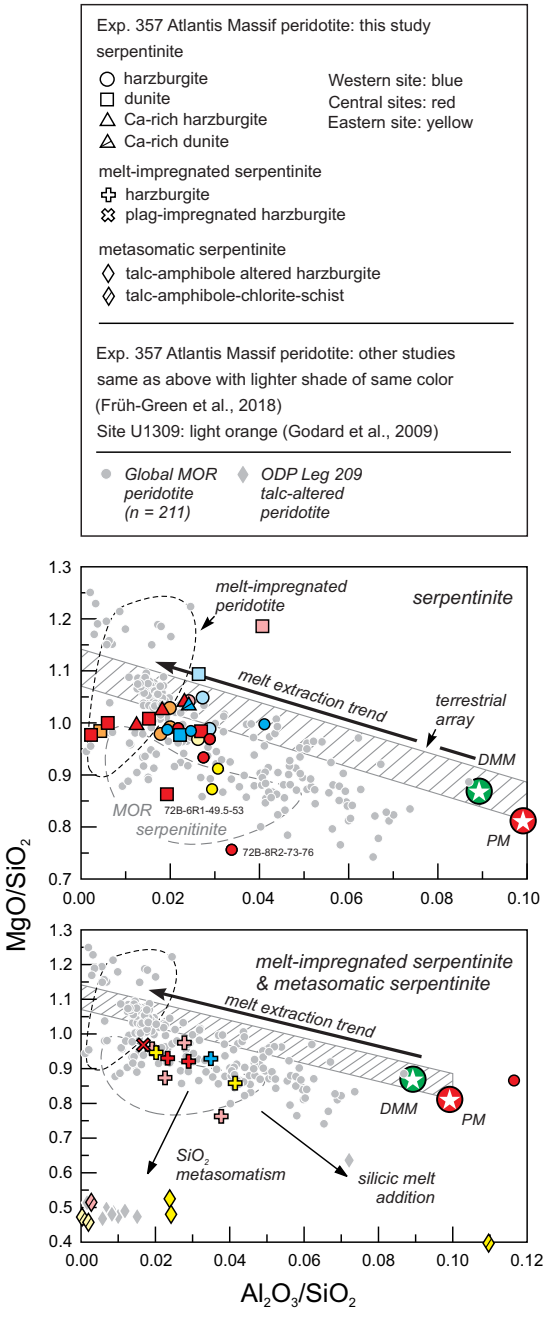

Figure 3 PR1 Whattam et al. (2021)

Figure 4

Click here to access/download;Figure;Fig. 4 PR2.pdf

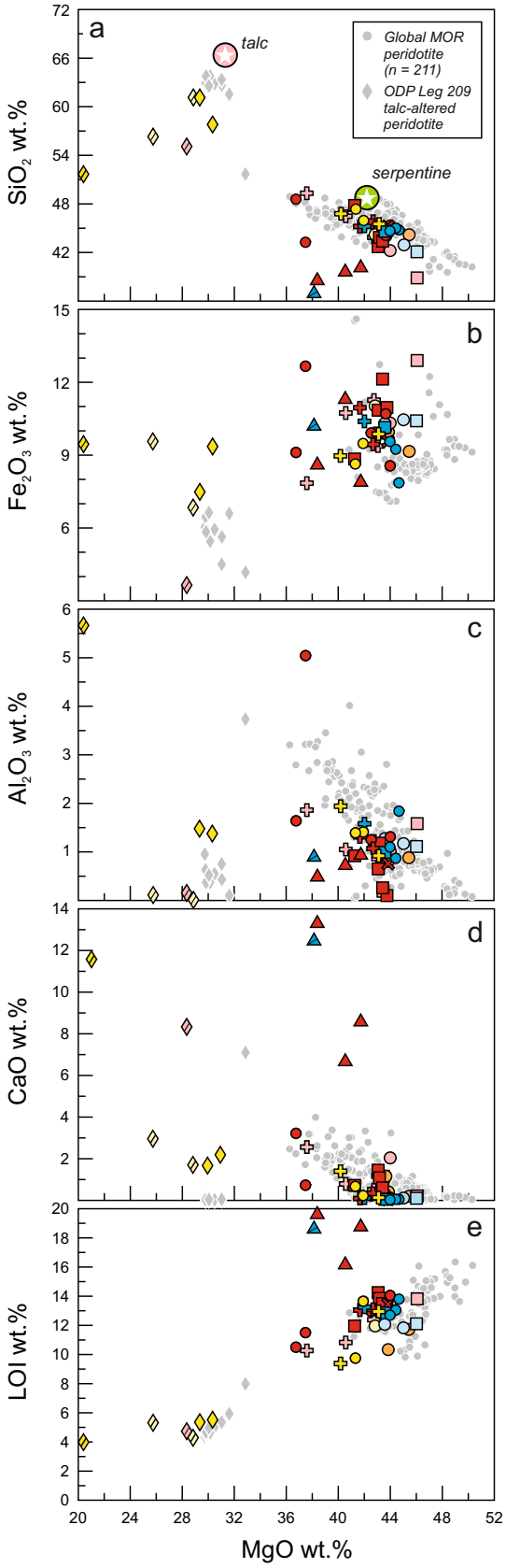

Figure 4 P-S 1A Whattam et al. (2021)

Figure 5

Click here to access/download;Figure;Fig. 5 PR2.pdf

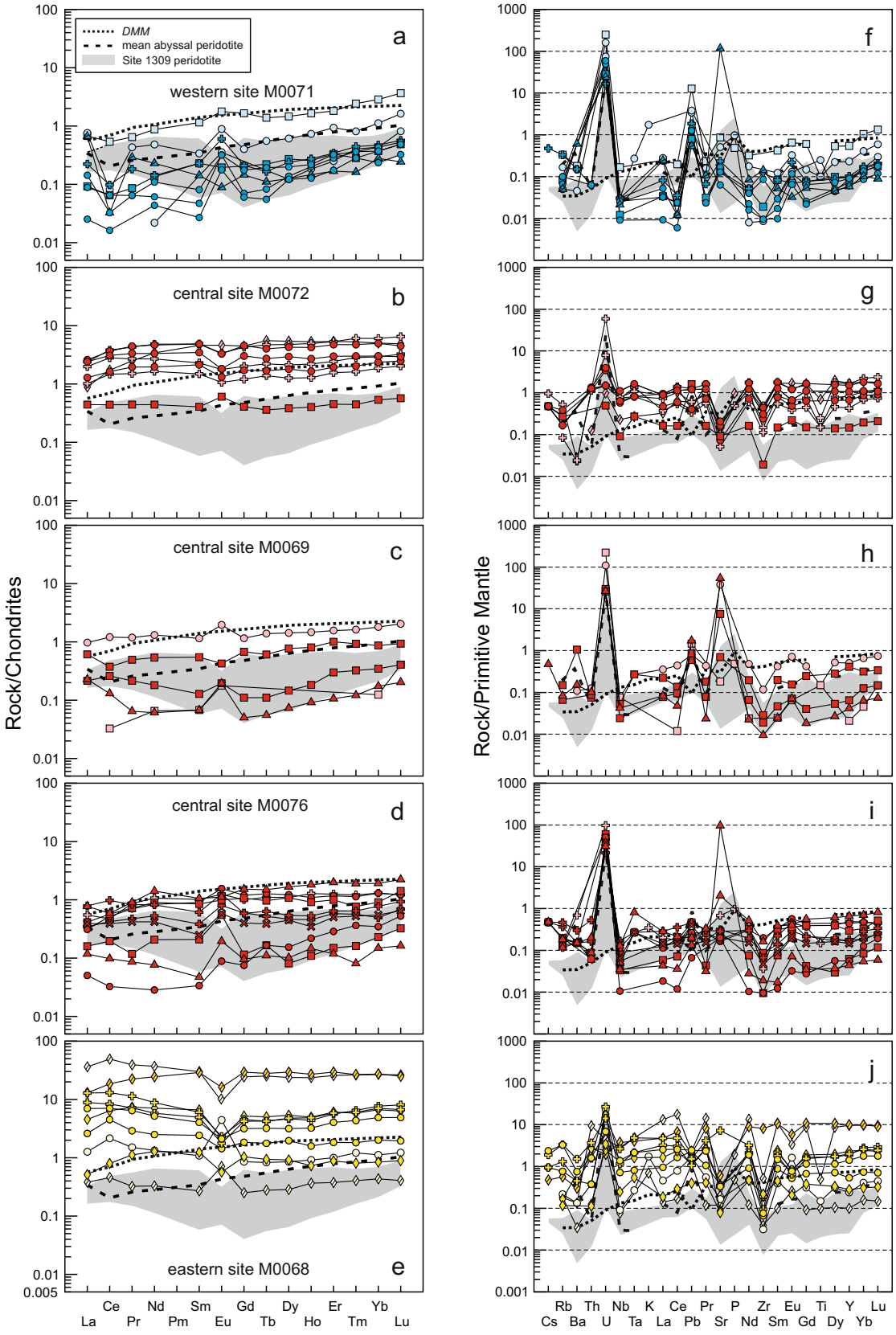

Figure 5 PR1 Whattam et al. (2021)

Figure 6

Click here to access/download;Figure;Fig. 6 PR2.pdf

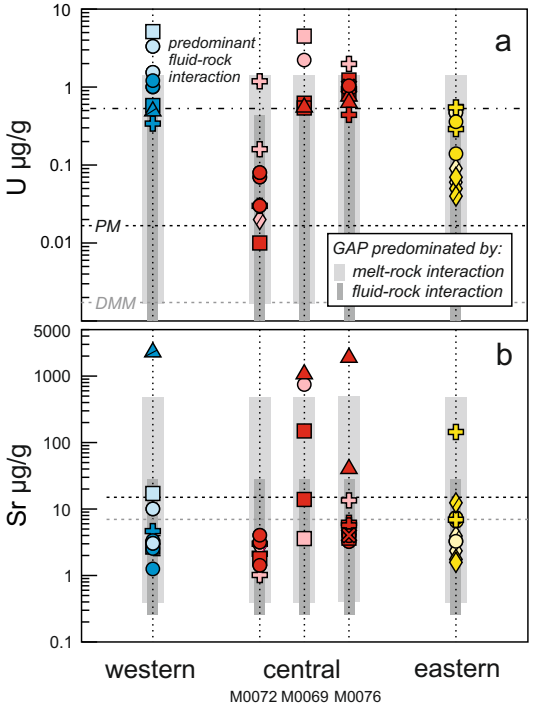

Figure 6 PR1 Whattam et al. (2021)

Figure 7

Click here to access/download;Figure;Fig. 7 PR2 .pdf

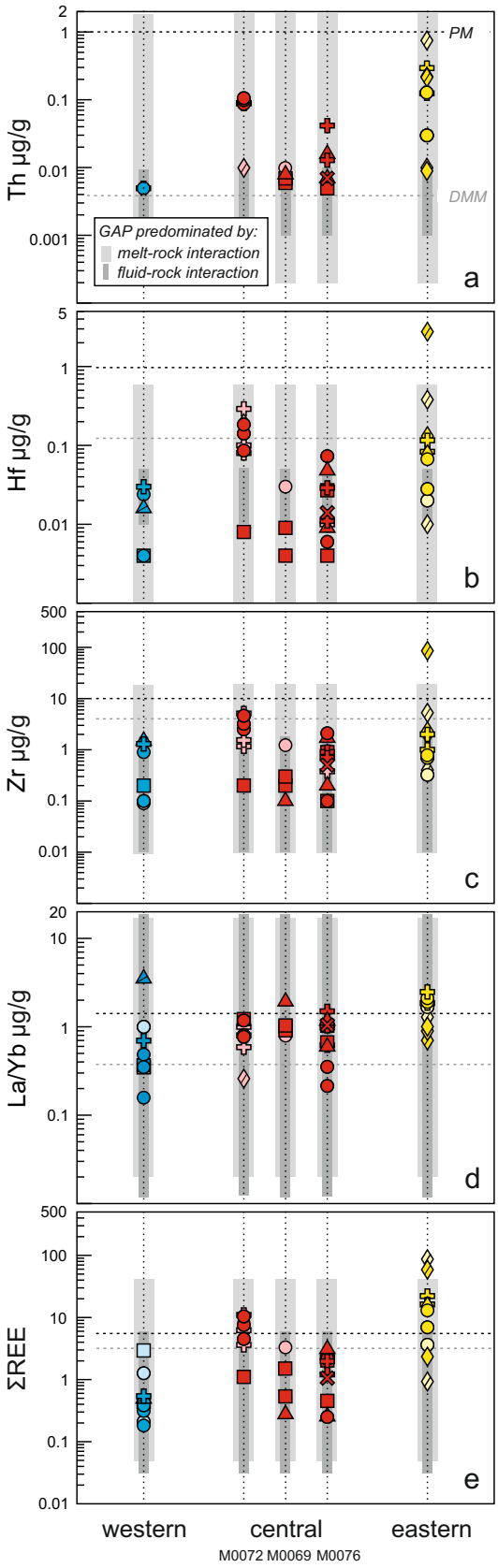

Figure 7 PR1 Whattam et al. (2021)

Figure 8

Click here to access/download;Figure;Fig. 8 PR2.pdf

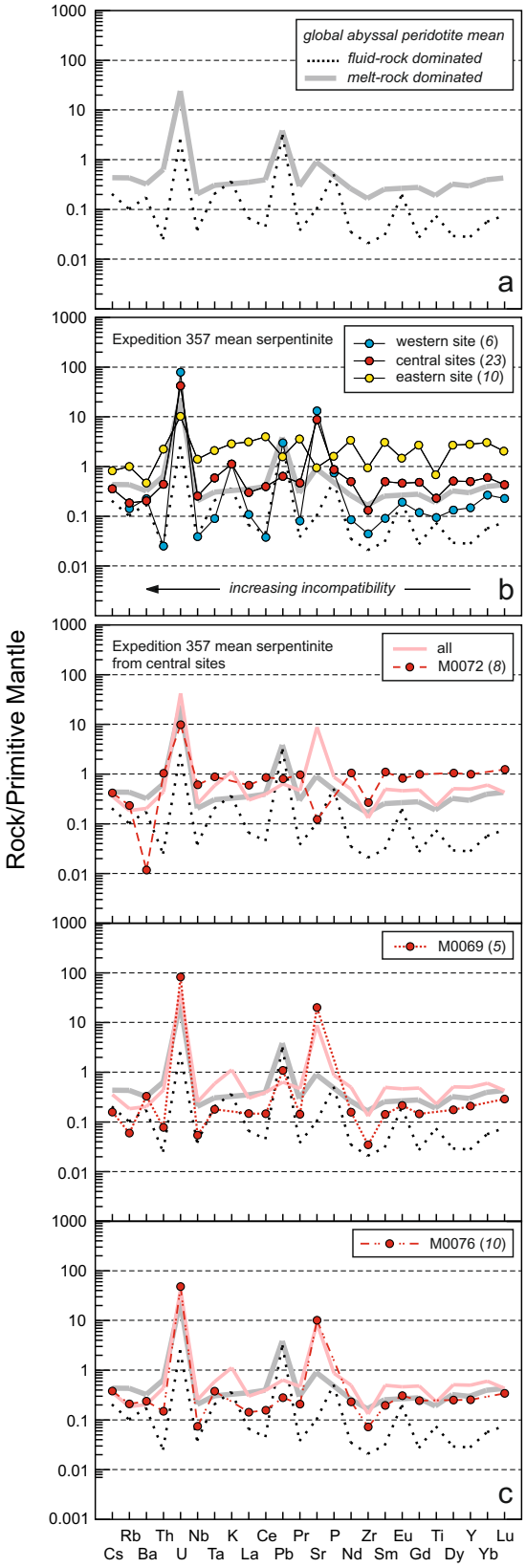

Figure 8 PR1 Whattam et al. (2021)

Figure 9

Click here to access/download;Figure;Fig. 9 PR2.pdf

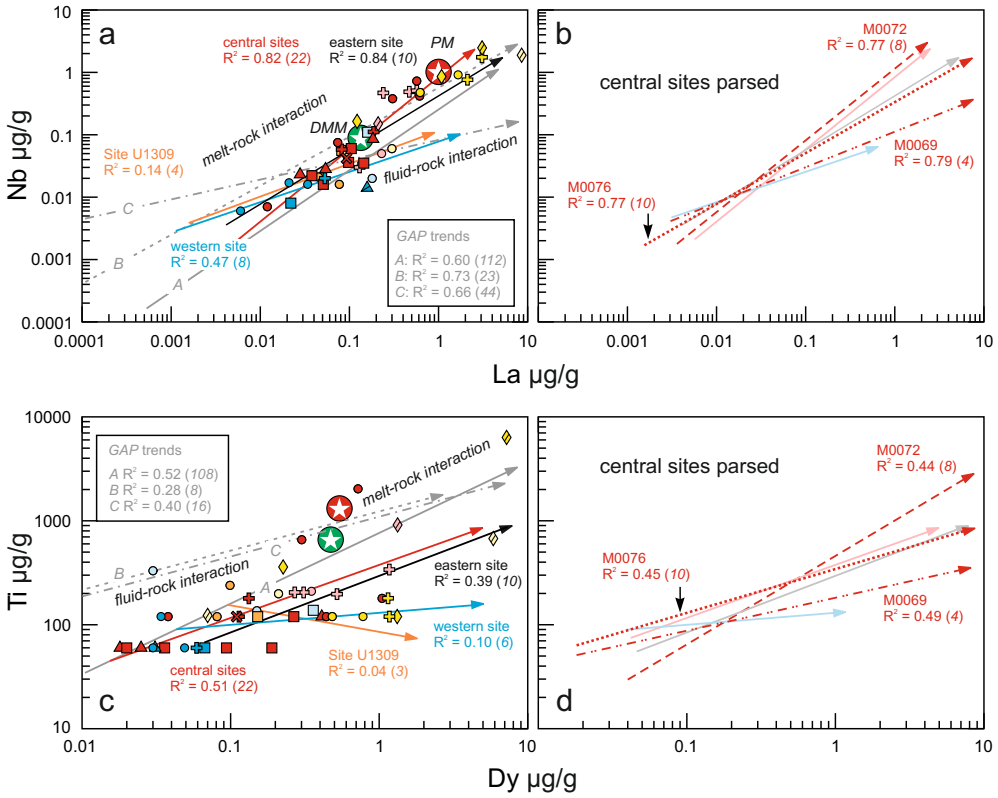

Figure 9 PR1 Whattam et al. (2021)

Figure 10

Click here to access/download;Figure;Fig. 10 PR2.pdf

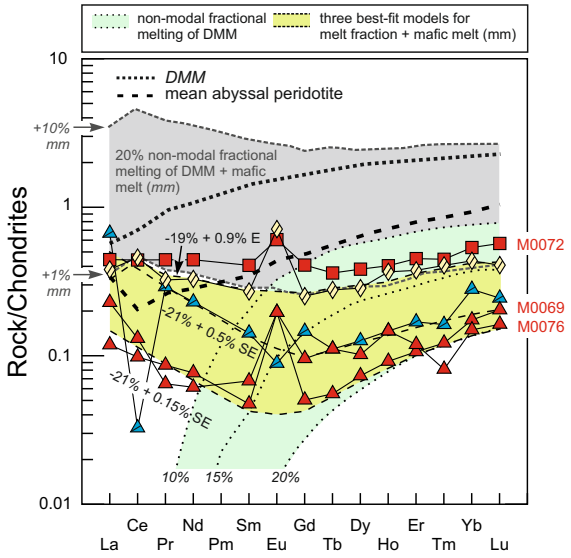

Figure 10 PR1 Whattam et al. (2021)

Table 1 Evidence and means for classisfication of Expedition 357 Atlantis Massif serpentinites subjected to melt-impregnation and (silica) metasomatism.

Site	Hole	Sample	Petrologic Type	Lithology	Evidence
western	M0071B	71B-1RCC-1-3	II	mm-i harzburgite	**macroscopic: presence of gabbro veins
central	M0072B	72B-7R1-76.5-79.5	II	*cryptically mm-i harzburgite	whole rock chemistry: incompatible element enrichment
		72B-8R2-23-26	II	cryptically mm-i harzburgite	whole rock chemistry: incompatible element enrichment
		72B-8R2-73-76	II	cryptically mm-i harzburgite	whole rock chemistry: incompatible element enrichment
	M0076B	76B-4R1-73-78	II	mm-i harzburgite	macroscopic: locally cut by mafic veins
		76B-6R1-65-68	II	mm-i harzburgite	macroscopic: presence of mafic melt intrusions
		76B-7R1-81-83	II	plagioclase-impregnated	petrographic: presence of rare plagioclase feldspar
eastern	M0068A	68A-1R1-1-6	III	talc-schist	petrographic: prevalence of secondary talc-amphibole whole rock chemistry: high SiO_2 (51.7 wt.%) , low MgO/SiO_2 (0.39), high Al_2O_3/SiO_2 (0.11)
	M0068B	68B-1R1-10-13	III	t-aa harzburgite	petrographic: talc-amphibole replacement of orthopyroxene whole rock chemistry: high SiO_2 (57.8 wt.%) , low MgO/SiO_2 (0.52)
		68B-4R1-23-29	II	mm-i harzburgite	petrographic: fresh olivine mantling orthopyroxene; olivine interpreted as recrystallized from mafic melt
		68B-4R1-45-49	II	mm-i harzburgite	macroscopic: presence of gabbro intrusions
		68B-6R1-8-10	III	t-aa harzburgite	petrographic: talc-amphibole replacement of orthopyroxene whole rock chemistry: high SiO_2 (61.1 wt.%) , low MgO/SiO_2 (0.48)

Notes:

Type I serpentinites (n = 20 of 29 total samples, see Table 3) are not listed as the only evidence for their classification is lack of melt-impregnation products and metasomatism. Type I includes the Ca-rich serpentinites (n = 4).

Abbreviations: mm-i, mafic melt-impregnated; t-aa, talc-amphibole altered.

Type II mm-i peridotite include plagioclase-impregnated peridotite.

*cryptically melt-impregnated refers to those peridotite which bear no evidence of impregnation at the scale of core or thin section (see text for further details).

**macroscopic evidence of mafic melt-impregnation determined by Expedition 357 Scientific Party at Onshore Scientific Party, University of Bremen, 2016 (see also Früh-Green et al., 2017, 2018).

Table 2 Mineralogy and modalogy of Expedition 357 serpentinites.

Informal sample no.	Hole	Core	Interval (cm)	Top depth (m)	Bottom depth (m)	Unit	Site	Petrologic Type*	Rock type	Modal proportions (%)***			Notes
										Ol	Opx	Spl****	
19-QU	M0071C	1R1	6-10	0	2.68	1	W	I	serpentinized harzburgite	85	15	1-2	Spl ranges up to 4 mm
5-GT	M0071C	5R1	6-8	7.38	9.63	1	W	I	serpentinized harzburgite	80	20	2-3	Spl usually embedded in Opx
10-GT	M0072B	8R2	23-26	10.71	12.43	1	C	I	serpentinized harzburgite	75	25	3	Spl embedded in Opx
7-GT	M0069A	9R2	8-12	13.04	14.72	1	C	I	Ca-rich harzburgite	90	10	0	secondary carbonate veinlets (sub-mm) comprises ~5% by volume
2-QU	M0069A	9R2	103-106	13.04	14.72	4	C	I	serpentinized dunite	100	0	0	
8-QU	M0076B	3R1	78-82	3.44	5.16	3	C	I	serpentinized dunite	100	0	<1	
13-QU	M0076B	5R1	59-61	6.73	7.98	1	C	I	serpentinized dunite	100	0	0	
15-QU	M0076B	6R1	65-68	7.98	9.72	1	C	II	mm-i harzburgite	70	30	0	
11-GT	M0076B	7R1	81-83	9.72	11.15	1	C	II	plag-impreg. harzburgite	85	15	0	Pl present only as two ~500 µm discrete grains
14-GT	M0076B	9R1	96-100	12.87	14.59	1	C	III	Ca-rich harzburgite	85	15	3	secondary carbonate veinlets (sub-mm) comprises ~10% by volume
6-GT	M0068B	1R1	10-13	0	1.72	1	E	III	t-aa harzburgite	70	30	2	Spl embedded in Opx
19-GT	M0068B	4R1	23-29	4	5.72	2	E	II	mm-i harzburgite	75	25	2-3	secondary (replacive) Ol comprises ~5% by volume
12-QU	M0068B	4R1	45-49	4	5.72	3	E	II	mm-i harzburgite	90	10	0	
18-GT	M0068A	1R1	1-6	0	1.97	1	E	III	talc schist**	-	-	0	

Notes:

Abbreviations: mm-i, mafic melt-impregnated; t-aa, talc-amphibole altered; GT-GemTek; QU, Queen's University.

*Petrologic Types: I, serpentinites; II, melt-impregnated serpentinites; III, metasomatic serpentinites.

Type I includes Ca-rich serpentinites; Type II includes plagioclase-impregnated (plag-impreg.) serpentinites.

**The high abundances of HFSE (e.g., Ti, Nb, Zr, see Table 3) suggests the protolith of the talc schist was mafic.

***Modal proportions of the protolith are visually estimated.

****Spl is usually sub-mm.

Table 3

Table 3 Whole rock chemical compositions of Expedition 357 serpentinites.

Hole	M0071C	M0071C	M0071C	M0071B	M0071A	M0071A	M0072B	M0072B	M0072B	M0072B	M0069A	M0069A	M0069A	M0076B	M0076B	M0076B	M0076B	M0076B	M0076B	M0076B	M0076B	M0076B	M0068B	M0068B	M0068B	M0068B	M0068B	M0068B	M0068A
Core	1R1	5R1	9R1	1RCC	1R1	1R2	6R1	7R1	8R2	8R2	9R2	9R2	10R2	3R1	4R1	4RCC	5R1	6R1	7R1	8R1	9R1	10R1	1R1	3R1	4R1	4R1	4R1	6R1	1R1
Interval (cm)	6-10	6-8	34-38	1-3	85-89	9-12	49.5-53	76.5-79.5	23-26	73-76	8-12	103-106	30-35	78-82	73-78	3-8	59-61	65-68	81-83	107.5-112.5	96-100	32.5-34.5	10-13	41-44	23-29	45-49	75-79	8-10	1-6
Top depth (m)	0	7.38	9.67	0	0	0	7.71	8.99	10.71	10.71	13.04	13.04	14.72	3.44	5.16	5.16	6.73	7.98	9.72	11.15	12.87	14.59	0	3.30	4	4	4	5.85	0
Bottom depth (m)	2.68	9.63	12.15	1.72	2.72	2.72	8.99	10.71	12.43	12.43	14.72	14.72	16.44	5.16	6.73	6.73	7.98	9.72	11.15	12.87	14.59	16.31	1.72	4	5.72	5.72	5.72	7.57	1.97
Unit	1	1	2	CC	2	MBIO	4	4	1	1	1	4	2	3	2	1	1	1	1	3	1	2	1	2	2	3	4	1	1
Site	W	W	W	W	W	W	C	C	C	C	C	C	C	C	C	C	C	C	C	C	C	C	E	E	E	E	E	E	E
Petrologic Type	I	I	I	II	I	I	I	I	I	I	I	I	I	I	I	I	I	II	II	I	I	I	III	I	II	II	I	III	III
Rock type (protolith)	serpentinized harzburgite	serpentinized harzburgite	serpentinized harzburgite	mm-i harzburgite	serpentinized dunite	Ca-rich dunite	serpentinized dunite	serpentinized harzburgite	serpentinized harzburgite	serpentinized harzburgite	Ca-rich harzburgite	serpentinized dunite	serpentinized dunite	serpentinized dunite	mm-i harzburgite	serpentinized harzburgite	serpentinized dunite	mm-i harzburgite	plag-impreg. harzburgite	Ca-rich harzburgite	Ca-rich harzburgite	serpentinized harzburgite	t-aa harzburgite	serpentinized harzburgite	mm-i harzburgite	mm-i harzburgite	serpentinized harzburgite	t-aa harzburgite	*talc schist
Major oxides wt.%																													
SiO_2	38.7	39.4	38.9	39.5	38.7	29.9	42.3	38.1	39.1	42.7	33.2	36.9	37.9	39.3	40.3	38.6	38.1	39.3	38.6	32.2	30.4	38.7	54.7	39.8	42.4	39.3	42.3	57.9	49.4
TiO_2	0.02	0.01	0.01	0.01	0.01	0.01	0.01	0.3	0.02	0.03	0.01	0.01	0.01	0.01	0.02	0.1	0.02	0.03	0.02	0.02	0.01	0.02	0.02	0.02	0.03	0.02	0.02	0.06	1.01
Al_2O_3	1.59	0.76	0.96	1.38	0.86	0.72	0.81	4.44	1.07	1.44	0.6	0.56	1.02	0.09	0.94	0.84	0.23	1.14	0.65	0.75	0.38	1.12	1.31	1.22	1.76	0.79	1.24	1.4	5.42
Fe_2O_3	6.79	8.09	8.33	9.08	8.8	8.26	7.82	11.15	8.51	8.01	9.47	9.37	8.56	9.62	8.3	9.37	10.65	9.52	8.16	6.33	6.78	7.3	8.85	8.21	8.13	8.52	7.71	7.08	9.04
CaO	0.04	0.04	0.03	0.1	0.04	10.1	0.64	0.64	0.19	2.83	5.59	1.25	0.93	0.07	0.3	0.07	0.53	0.08	0.04	6.88	10.5	0.12	0.57	0.2	1.27	0.11	0.6	0.08	9.56
MgO	38.6	38.9	38.3	36.7	37.8	30.9	36.5	33	36.5	32.3	34	37.2	37.3	38.4	37.5	38.2	38.1	36.2	37.4	33.5	30.3	37.5	28.7	36.3	36.4	37.2	36.9	27.8	19.5
Na_2O	0.15	0.06	0.07	0.18	0.13	0.15	0.06	0.08	0.04	0.19	0.19	0.2	0.16	0.11	0.09	0.12	0.02	0.12	0.04	0.06	0.12	0.07	0.16	0.24	0.23	0.08	0.13	0.13	1.08
K_2O	0.03			0.04	0.03	0.02					0.02	0.02	0.03					0.05					0.03	0.05	0.15	0.08	0.12	0.03	0.08
Cr_2O_3	0.44	0.23	0.43	0.28	0.3	0.58	0.27	0.26	0.34	0.31	0.63	0.31	0.39	0.07	0.32	0.18	0.04	0.39	0.34	0.22	0.18	0.36	0.23	0.36	0.1	0.12	0.2	0.16	0.14
MnO	0.08	0.07	0.07	0.07	0.07	0.14	0.08	0.08	0.08	0.09	0.06	0.56	0.09	0.13	0.11	0.06	0.1	0.09	0.08	0.32	0.05	0.07	0.05	0.19	0.12	0.08	0.11	0.05	0.18
P_2O_5				0.01	0.01	0.03					0.01	0.02	0.01						0.01	0.02	0.02	0.01	0.01	0.03	0.01	0.01		0.02	0.12
LOI	13.8	13.05	12.7	13.25	12.85	18.6	11.95	11.5	12.95	10.5	16.15	14.25	13.85	13.35	13.1	13.55	13.5	13.05	13.45	18.75	19.6	14.05	5.51	13.65	9.38	12.95	9.75	5.35	3.98
Total %	100.24	100.61	99.8	100.6	99.6	99.64	100.44	99.58	98.8	98.4	100.05	100.65	100.27	101.15	100.98	101.09	101.29	99.97	98.79	99.05	98.55	99.32	100.14	100.27	100	99.26	99.08	100.06	99.51
Mg#	*91.8*	*90.5*	*90.1*	*88.9*	*89.5*	*88.1*	*90.2*	*85.4*	*89.5*	*88.9*	*87.7*	*88.7*	*89.6*	*88.8*	*89.9*	*89*	*87.6*	*88.3*	*90.1*	*91.3*	*89.8*	*91.1*	*86.5*	*89.8*	*89.9*	*89.6*	*90.5*	*88.6*	*81.0*
MgO/SiO $_2$	*1.00*	*0.99*	*0.98*	*0.93*	*0.98*	*1.03*	*0.86*	*0.87*	*0.93*	*0.76*	*1.02*	*1.01*	*0.98*	*0.98*	*0.93*	*0.99*	*1.00*	*0.92*	*0.97*	*1.04*	*1.00*	*0.97*	*0.52*	*0.91*	*0.86*	*0.95*	*0.87*	*0.48*	*0.39*
Al $_2O_3/SiO_2$	*0.04*	*0.02*	*0.02*	*0.03*	*0.02*	*0.02*	*0.02*	*0.12*	*0.03*	*0.03*	*0.02*	*0.02*	*0.03*	*0.00*	*0.02*	*0.02*	*0.01*	*0.03*	*0.02*	*0.02*	*0.01*	*0.03*	*0.02*	*0.03*	*0.04*	*0.02*	*0.03*	*0.02*	*0.11*
Trace elements (µg/g)																													
Sc	14.55	9.67	8.69	10.65	9.54	3.63	8.31	14.85	9.16	10.25	3.9	6.56	10.15	2.9	6.66	6.37	2.67	9.84	5.47	7.11	4.99	11.35	8.53	9.32	4.66	4.52	9.84	6.72	31.2
V	74.3	36.2	37.3	52.4	39.4	45.1	24.5	85.1	32.2	38.1	28.7	28.2	33.5	20.9	37	36.8	18.1	53.9	36.5	32.5	14.5	39.2	29.6	44.8	12.9	11.3	33.9	29.1	174.5
Cr	1900	1015	1670	1325	1145	2620	1250	1395	1715	1650	2840	1295	1640	292	1385	793	168.5	1635	1755	849	738	1500	1085	1325	398	409	1060	757	706
Ni	1290	1700	2630	1210	1720	1030	2130	1915	2080	2010	2210	2270	1925	2000	1995	1705	1820	1910	2210	1590	1930	2270	1250	1510	2200	2050	2180	1275	698
Li	1.6	5.2	1.4	10.8	2.9	0.4	1.6	6.5	1.3	1.1	0.8	2.8	5.2	5.5	6.7	2.2	1.4	6.4	4.7	2.3	1.2	3.5	3.5	18.1	7.7	5.5	7.3	8	19.6
Co	68	63.8	110.5	81.1	84.1	96.1	93.3	112.5	100.5	91.4	114	107.5	84.7	90.8	87.1	49.2	70.8	104	113.5	67	78.9	102	64.4	99.3	116.5	97	106	75.9	51.3
Cu	14.4	18.85	44.4	28.9	9.95	8.84	0.54	3.04	0.69	0.75	5.24	2.05	1.97	2.18	1.83	54	1.73	1.13	2.12	2.25	2.76	2.71	33.1	28.4	8.36	7.06	9.2	0.4	109
Zn	54.7	42.1	54.1	50.8	40.3	195.5	12.2	18.1	15.6	12	49.4	34.1	39	29.1	25.9	23.3	21.9	25.4	29.3	17.4	29.5	35.3	36.7	102.5	49	46	46.1	51.2	69.4
Ga	1.48	0.72	0.94	2.18	1.12	1.02	1.61	5.77	1.96	2.61	1.6	1.14	1.16	0.36	1.66	1.97	0.52	1.64	1.29	0.96	0.47	1.06	2.65	1.89	3.19	1.77	2.12	2	11
Rb	0.04	0.06	0.06	0.2	0.05	0.03	0.16	0.1	0.17	0.23	0.05	0.09	0.04	0.11	0.22	0.12	0.08	0.28	0.12	0.11	0.07	0.08	0.1	0.46	2.01	0.79	1.98	0.07	0.34
Sr	3.37	2.56	1.26	4.68	2.69	2320	1.82	4.1	1.44	3.22	1080	14	150.5	5.31	6.24	3.26	3.67	5.71	4.06	40.6	1925	4	1.75	7.42	145	6.91	6.64	1.58	12.45
Y	0.31	0.39	0.26	0.44	0.39	0.25	0.63	4.53	2.86	6.44	0.18	1.77	0.28	0.27	0.78	1.9	1.28	0.68	0.63	2.84	0.19	0.24	10.15	2.32	8.23	8.66	6.13	1.21	42.7
Zr	0.1	0.9	0.1	1.3	0.2	1.5	0.2	3.2	2.5	4.6	0.1	0.3	0.2	0.1	0.9	2.1	0.9	0.7	0.5	1.7	0.2	0.1	2	0.7	1	2	0.8	2.3	85.6
Nb	0.016	0.017	0.006	0.02	0.008	0.014	0.06	0.726	0.378	0.417	0.028	0.035	0.016	0.022	0.058	0.075	0.036	0.111	0.042	0.085	0.023	0.007	0.855	0.476	1.75	0.763	0.914	0.164	2.47
Mo	0.36	0.09	0.21	0.31	0.17	1.68	0.04	0.12	0.11	0.07	0.3	1.37	0.42	0.98	0.52	0.31	0.49	0.19	0.41	0.62	0.12	0.07	0.09	0.84	0.2	0.16	0.17	0.03	0.22
Cd	0.032	0.021	0.005	0.024	0.028	0.015	<0.005	0.007	<0.005	0.007	0.008	0.019	0.011	0.03	0.056	0.024	0.032	0.03	0.027	0.193	0.013	0.025	<0.005	0.036	0.045	0.041	0.03	0.011	<0.005
Sn	0.14	0.06	0.07	0.24	0.05	0.1	0.06	0.27	0.14	0.3	0.24	0.07	0.12	0.06	0.07	0.12	0.08	0.1	0.08	0.1	0.11	0.13	0.8	0.69	1.31	0.98	1.48	0.12	3.46
Sb	0.37	0.14	0.04	0.46	0.2	1.04	0.05	0.06	0.04	0.03	0.04	0.08	0.09	0.27	0.08	0.19	0.07	0.03	<0.02	0.08	0.08	0.1	0.06	0.4	0.13	0.08	0.08	0.03	0.07
Cs	<0.01	<0.01	<0.01	0.01	<0.01	<0.01	0.01	0.01	0.01	0.01	0.01	<0.01	<0.01	<0.01	0.01	<0.01	<0.01	0.01	0.01	0.01	<0.01	<0.01	<0.01	0.02	0.04	0.02	0.05	<0.01	0.01
Ba	<1	<1	<1	1	<1	4	<1	<1	<1	<1	1	7	<1	1	1	<1	1	2	1	1	1	<1	<1	3	10	3	5	<1	2
La	0.034	0.021	0.006	0.053	0.022	0.158	0.105	0.57	0.305	0.615	0.054	0.145	0.051	0.038	0.082	0.074	0.098	0.187	0.093	0.184	0.028	0.012	1.08	0.621	3.07	2.11	1.66	0.122	3.08
Ce	0.02	0.04	0.01	0.06	0.04	0.02	0.27	1.89	1	2.24	0.08	0.23	0.16	0.12	0.26	0.32	0.35	0.6	0.24	0.36	0.06	0.02	3.93	2.77	8.04	5.12	4.33	0.49	11.35
Pr	0.006	0.006	bdl	0.017	0.008	0.027	0.041	0.309	0.181	0.411	0.006	0.046	0.02	0.011	0.044	0.065	0.067	0.077	0.039	0.084	0.008	bdl	0.686	0.27	1.06	0.669	0.6	0.104	2.08
Nd	0.028	0.05	0.02	0.065	0.062	0.105	0.202	1.52	0.895	2.13	0.028	0.246	0.083	0.095	0.243	0.383	0.412	0.376	0.192	0.647	0.035	0.013	3.25	1.145	4.04	2.66	2.38	0.585	11.2
Sm	0.007	0.012	0.004	0.034	0.034	0.021	0.06	0.512	0.315	0.718	0.01	0.081	0.019	0.031	0.057	0.134	0.126	0.091	0.037	0.157	0.007	0.005	0.982	0.36	0.893	0.733	0.601	0.184	4.29
Eu	0.018	0.018	0.01	0.034	0.011	0.005	0.034	0.102	0.074	0.186	0.011	0.024	0.011	0.031	0.045	0.088	0.056	0.071	0.033	0.063	0.011	0.005	0.122	0.081	0.131	0.1	0.119	0.032	0.912
Gd	0.014	0.035	0.012	0.042	0.041	0.029	0.081	0.599	0.343	0.903	0.01	0.135	0.022	0.023	0.119	0.239	0.213	0.117	0.08	0.304	0.019	0.015	1.035	0.367	0.905	0.843	0.63	0.207	5.86
Tb	0.003	0.007	0.002	0.006	0.008	0.004	0.013	0.098	0.061	0.145	0.002	0.022	0.004	0.006	0.019	0.046	0.035	0.023	0.014	0.054	0.004	0.006	0.182	0.064	0.153	0.154	0.116	0.034	1.01
Dy	0.034	0.049	0.03	0.059	0.067	0.031	0.094	0.723	0.442	1.05	0.018	0.19	0.036	0.02	0.114	0.302	0.267	0.133	0.11	0.412	0.025	0.038	1.325	0.484	1.15	1.175	0.78	0.226	7.23
Ho	0.011	0.012	0.007	0.015	0.014	0.008	0.022	0.147	0.09	0.231	0.005	0.044	0.01	0.006	0.025	0.06	0.05	0.029	0.019	0.099	0.008	0.012	0.272	0.087	0.24	0.266	0.177	0.04	1.475
Er	0.045	0.052	0.028	0.055	0.053	0.027	0.072	0.477	0.309	0.756	0.017	0.161	0.048	0.024	0.093	0.188	0.16	0.103	0.081	0.319	0.019	0.046	0.975	0.294	0.902	0.938	0.649	0.141	4.72
Tm	0.009	0.009	0.007	0.011	0.007	0.004	0.011	0.074	0.05	0.117	0.003	0.023	0.008	0.004	0.014	0.028	0.019	0.016	0.013	0.047	0.002	0.009	0.144	0.045	0.161	0.149	0.108	0.02	0.66
Yb	0.07	0.06	0.038	0.076	0.06	0.045	0.086	0.484	0.38	0.798	0.028	0.14	0.056	0.037	0.08	0.21	0.147	0.125	0.089	0.309	0.024	0.056	1.075	0.325	1.24	1.14	0.79	0.136	4.4
Lu	0.013	0.012	0.008	0.014	0.012	0.006	0.014	0.072	0.061	0.111	0.005	0.023	0.01	0.008	0.017	0.03	0.035	0.023	0.016	0.055	0.004	0.013	0.156	0.048	0.199	0.165	0.121	0.022	0.617
Hf	0.004	0.024	<0.004	0.03	0.004	0.016	0.008	0.141	0.086	0.184	<0.004	0.009	0.004	0.004	0.029	0.073	0.027	0.011	0.014	0.048	0.009	0.006	0.131	0.028	0.083	0.116	0.067	0.077	2.76
Ta	<0.01	<0.01	<0.01	<0.01	<0.01	<0.01	0.01	0.06	0.03	0.03	<0.01	0.01	<0.01	<0.01	<0.01	0.01	<0.01	0.01	0.01	0.03	<0.01	<0.01	0.06	0.03	0.18	0.08	0.08	0.02	0.15
Pb	0.21	0.18	0.19	0.28	0.12	0.08	0.24	0.18	0.06	0.06	0.26	0.09	0.13	0.07	0.02	0.04	0.03	0.07	0.06	0.03	0.02	0.01	0.17	0.34	0.23	0.16	0.37	0.06	0.3
Th	<0.004	0.005	<0.004	0.005	<0.004	<0.004	<0.004	0.1	0.088	0.107	0.008	0.006	0.007	<0.004	0.013	0.005	0.005	0.042	0.007	0.016	0.007	<0.004	0.215	0.03	0.294	0.125	0.128	0.009	0.221
U	1	1.01	1.21	0.34	0.58	0.49	0.01	0.03	0.07	0.08	0.54	0.61	0.53	1.23	0.94	0.91	0.82	0.44	1.01	0.76	0.63	1.04	0.05	0.36	0.29	0.55	0.14	0.07	0.04

Notes:

bdl, below detection limit.

abbreviations: mm-i, mafic melt-impregnated; t-aa, talc-amphibole altered.

Type I serpentinites include Ca-rich serpentinites; Type II mm-i serpentinites include plagioclase-impregnated (plag-impreg.) serpentinites.

*Protolith of the schist is probably mafic (compare HFSE concentrations with remaining samples).

Supplementary file

Click here to access/download
Supplementary file
Archive.zip

Declaration of interests

☒ The authors declare that they have no known competing financial interests or personal relationships that could have appeared to influence the work reported in this paper.

☐The authors declare the following financial interests/personal relationships which may be considered as potential competing interests: